UNIVERSITY OF OSLO
Department of physics

Master's Thesis

Synthesis and Characterization of Homoepitaxial ZnO Thin Films

Vegard Skiftestad Olsen

A thesis submitted in fulfilment of the requirements for the degree of MSc

in

Materials, Energy and Nanotechnology

May, 2015

Abstract

ZnO is especially interesting due to its large and direct bandgap and large exciton binding energy (60 meV) which gives the material potential for LED- and laser applications. The biggest obstacle for ZnO is the lack of stable and reproducible p-type conductivity. Many research groups all over the world has combated this problem, since for LED applications both n- and p-type ZnO is necessary. Some groups have also reported positive results in terms of p-type ZnO. In terms of solar cells, ZnO, due to its transparency, can be used as a transparent conductive oxide (TCO) which can act as the front contact of the solar cell. Clearly, zinc oxide has several applications and great effort is put into realizing improvements, both in terms of technology and costs. One improvement, serving all applications, is the realization of homoepitaxial growth of ZnO. The epitaxial growth of ZnO is mainly done by Molecular Beam Epitaxy (MBE) and Metal-Organic Chemical Vapor Deposition (MOCVD), both expensive growth techniques. Sputtering on the other hand is a technique used widely for industrial production of zinc oxide thin films, and is a relatively cheap method compared to the two mentioned above. In this study, ZnO thin films were deposited using sputter deposition and both deposition power (10W - 110W) and temperature (400°C and 600°C) were varied to obtain homoepitaxial growth. Low deposition powers was found to give excellent crystal quality with a minimum XRD rocking curve FWHM of 0.010° for 10W 400°C and 30W 600°C, and yielding epitaxial growth within grains as evidenced by XRD-, PL-, RBS- and AFM characterizations. A significant increase in grain size was observed for increasing deposition temperature.

Acknowledgements

I would like to thank my supervisor Prof. Edouard Monakhov for giving me the opportunity of doing this study. His expertise and knowledge of the field of semiconductors, in addition to the always helpful advices he has given me, have helped me tremendously.

Special gratitude goes to my co-supervisor Heine N. Riise, who has been my day-to-day supervisor and has always kept his door open for me and my endless questions. I appreciate the introduction he has given me to various experimental methods. Finally, for all the time he has spent discussing results and proof-reading my thesis, in addition to all the advises he has given me, my gratitude can not be expressed enough.

I would like to thank Dr. Augustinas Galeckas for PL measurements, Dr. Alexander Azarov for RBS measurements and Thomas Neset Sky for SIMS measurements. The time the three of you also spent on discussing the results with me, helped me a great deal. Thanks to Ass. Prof. Lasse Vines and Oddvar Dyrlie for teaching me how to use AFM.

A special thanks also goes to Viktor Bobal and Mikael Sjödin for helping me when problems with the instruments at MiNaLab occurred. Many hours of frustration were prevented with your help. To all my fellow master students and all the employees at LENS, I would like to thank each and every one of you for making these years so inspiring, stimulating and fun.

Finally, to all my friends and family who have supported me all my life, I owe you my deepest gratitude. I am very grateful for all the love and inspiring words you have given me.

Contents

Chapter 1

Introduction

In a world where nanotechnology no longer is a strange and frightening future, the technology is present in our daily lives. Devices such as mobile phones and computers, could never be as technologically advanced or cheap if not for nanotechnology. The worlds increasing need for energy, and the environmental consequences of that energy production, represent two of the biggest challenges humanity faces today. Reducing CO_2 emission and making renewable energy the main energy source is necessary. By the end of 2013 140 million tonnes of CO_2 per year were avoided by generating 160 TWh/year of clean energy [1].

The solar photovoltaic (PV) effect makes it possible to extract energy from the sun, our largest source of energy. So, what's the problem? Why cannot mankind base its energy-use on power extracted from the sun? There are several reasons why solar cells are not the main energy source, but the main one is the cost vs. efficiency problem. In certain regions of the world the percentage of solar energy which can be converted to electrical power does not justify the cost of producing the solar cells, installation and maintenance. Semiconductor physicists worldwide are constantly working on improving device efficiencies and realizing new and better devices by introducing new materials. One exciting group of materials is the functional oxides, of which zinc oxide (ZnO) is an example of these. ZnO is relatively cheap, since both oxygen and zinc are elements the world possesses at a large scale. The International Zinc Association (IZA) has estimated that the first mile of the earth's crust under land contains 224,000,000 million tonnes of zinc [2].

ZnO can be used as transparent conductive oxide (TCO) in solar cells, with the purpose of being the top electrode. The transparency of the material results in a larger area of the solar cell being exposed to light compared to thin metal contact fingers. Another common application of semiconductor materials is diodes. Light emitting diodes (LED) are sources of light used as traffic signals or the illumination source in TVs to name a few. ZnO has the potential of realizing blue LED and laser devices based on excitonic photon emission. Although zinc oxide has several present- and future applications, certain challenges are associated with the material. The most challenging problem is the lack of a low resistive and stable p-type state, although many research groups have reported promising results [3,4]. For ZnO to release its potential in blue LEDs, TCOs or other applications, the ability of growing it homoepitaxially is a significant advantage. Such growth has also been achieved, though mostly using Metal-Organic Chemical Vapor Deposition (MOCVD) or Molecular Beam Epitaxy (MBE) [5] which are expensive deposition techniques. A relatively cheap way to make thin films is by

using sputter deposition, and this technique is commonly used in industry. Since sputter deposition is based on relatively high energetic atoms and molecules bombarding the substrate, the deposition method yields polycrystalline thin films. The question then remains: **can ZnO be grown homoepitaxially using sputter deposition, giving a cost reducing alternative for high quality thin film processing?** In this study mainly sputter parameters such as deposition power and substrate temperature have been varied for obtaining such films.

Thesis thesis consists of five chapters. The first chapter is theory, where the theory of crystalline materials, semiconductors and ZnO is presented. The following chapter explains the experimental techniques used in this study. In the results chapter, the results obtained in this study are presented with some minor discussions, before the results are discussed and concluded in the discussion- and conclusion chapter, respectively.

The results obtained from the power series have been presented at European Materials Research Society (EMRS) 2015 spring meeting and are in preparation for publishing in the journal *Thin Solid Films*.

Chapter 2

Theory

2.1 Crystalline Materials

This section is based on the textbooks of Streetman and Banerjee [6], Tilley [7] and Müller [8]. Solids can be composed of one single crystal (*crystalline solids*), several small crystals (*polycrystalline solids*) or the material can have no periodic arrangement (*amorphous solids*). In a crystalline material the atoms are arranged in a periodic fashion, called the crystal structure. The periodicity within the crystal is termed the lattice, which is an array of symmetric points. Thus if a randomly selected lattice point is chosen as origin, the position of any other lattice point is given by:

$$\mathbf{P}(uvw) = u\mathbf{a} + v\mathbf{b} + w\mathbf{c} \tag{2.1}$$

where **a**, **b** and **c** are basis vectors and u,v and w are positive or negative integers. The cell spanned by these vectors when u,v,w=1 is the *unit cell* of the lattice, and is the smallest repeatable cell with dimensions ($|\mathbf{a}| = a_0$, $|\mathbf{b}| = b_0$, $|\mathbf{c}| = c_0$). The unit cell always contains an integer number of atoms, e.g. each of the 8 corner atoms of a unit cell is shared with 7 other unit cells, and the sum of corner atoms in a single unit cell equals one atom. There are 14 different three-dimensional lattices coined *Bravais lattices*. Within each Bravais lattice, there can be different variants; besides from the *simple* (or primitive) unit cell, the cell can be *body-centered* (an atom in the center of the cell), *face-centered* (an atom in the center of each side of the cell) or *base-centered* (an atom in the center at the top- and bottom side of the cell). There are 7 crystal structures, and 32 crystal classes. Each of these 32 crystal classes are appointed their own crystallographic point group, which relates the internal and external symmetry to the observable physical properties of the material. By combining the symmetry of the point group with the three dimensional symmetry of the lattice, 230 possible combinations are obtained, called *space groups*.

Miller indices are used to identify the different planes throughout the crystal and the indices (hkl) define a set of parallel planes. By finding at which point the plane intercepts the primitive lattice vectors **a**, **b** and **c** (for example at 1**a** and 1**b**, while it never intercepts with **c**) and by taking the reciprocal of these values (1/1, 1/1, $1/\infty$), the indices of the plane is obtained ((110)). The vector [110] is perpendicular to the plane (110). For hexagonal crystal structures the *Miller-Bravais indices* (hkil) are used, where

$$i = -(h + k)$$

In contrast to gases and liquids, atoms and molecules in solids are strongly bound together. The three main types of bonds in solids are covalent-, ionic- and metallic bonds, while for semiconductors the bonds are covalent, ionic or a combination of these. A covalent (or electron-pair) bond occurs when two atoms with unpaired electrons interact. The two previously unpaired electrons are thus shared in a molecular orbital, the covalent bond. Ionic bonds consists of ions with opposite charges. The ions are held together by an electrostatic attraction, and the distance between the ions is a compromise between this attraction and the repulsion from interacting electron clouds.

2.2 Semiconductors

This section is based on the textbooks of Streetman [6], Kittel [9], Hemmer [10] and Griffiths [11]. Semiconductor materials have electrical conductivities between metals and insulators and can be divided into two main groups; *elemental semiconductors* composed of a single element such as silicon, and *compound semiconductors* consisting of two or more elements such as zinc oxide. The electrical conductivity of a semiconductor can be varied as a function of temperature and optical excitation intensity or by introducing impurities. These materials can be used in several applications since their electrical properties can be tailored to that application's specific needs. Typical applications for semiconductors are solar cells, transistors and diodes.

2.2.1 Energy bands

An isolated atom possesses several discrete energy levels, and some of these are filled with electrons. The energy levels which are either fully or partially filled, contains electrons called valence electrons. In solids, where the number of atoms is high (about Avogadro's number $\sim 10^{23}$), the electron energy levels are no longer discrete.

The large number of atoms bound together result in a periodic potential. A single electron's interaction with other electrons can be approximated by what is known as a nearly-free electron. The time-independent Schrödinger equation for the periodic potential in a solid can be expressed as;

$$H\Psi(\mathbf{r}) = [-\frac{\hbar}{2m}\nabla^2 + U(\mathbf{r})]\Psi(\mathbf{r}) = \epsilon\Psi(\mathbf{r}) \tag{2.2}$$

Where H is the Hamilton operator, $\Psi(\mathbf{r})$ is the electron wave function, m is the electron mass, U($\mathbf{r}$) is the periodic potential and ϵ is the energy eigenvalue for the given potential. The periodicity of the potential is expressed by a Bloch function. If both dislocations and thermal vibrations are neglected the potential is periodic, i.e.

$$U(\mathbf{r} + \mathbf{R}) = U(\mathbf{r}) \tag{2.3}$$

which means that the eigenfunction of equation (2.2) has the form

$$\Psi_{\mathbf{k}}(\mathbf{r}) = e^{i\mathbf{kr}}u_{\mathbf{k}}(\mathbf{r}) \tag{2.4}$$

where $\mathbf{k}$ is the wave vector, and $u_{\mathbf{k}}(\mathbf{r})$ has the same periodicity as the lattice, i.e.

$$u_{\mathbf{k}}(\mathbf{r} + \mathbf{R}) = u_{\mathbf{k}}(\mathbf{r}). \tag{2.5}$$

The energy eigenvalue, ϵ, in equation (2.2) is dependent of $\mathbf{k}$ and gives the allowed energy states of the electron. For this periodic potential in a finite volume, it is expected that for each $\mathbf{k}$, ϵ_n (Where n is the band index (n = 1, 2, 3,..), see figure 2.1) will have discrete levels which can vary with $\mathbf{k}$. The bands can be separated by gaps of forbidden states, called band gaps (E_g). The highest occupied band at 0K is called the *valence band* (E_v), while the lowest unoccupied band at 0K is the *conduction band* (E_c). The creation of energy bands can also be

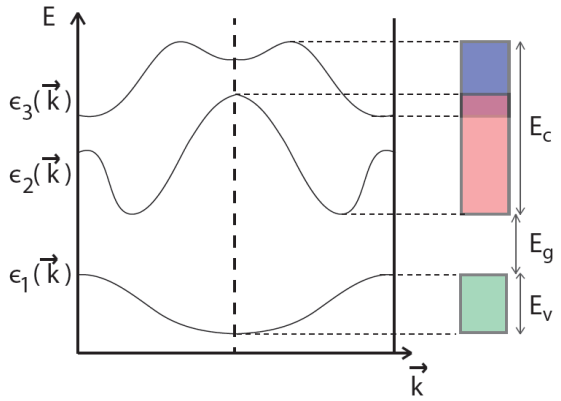

Figure 2.1: *Eigenvalues, ϵ_n, as a function of $\mathbf{k}$. The energy gap between the valence band and the conduction band is called the band gap. Figure adapted from Hemmer [10].*

visualized by building the crystal atom by atom. When two atoms are bound together, Pauli's exclusion principle prohibits the two electrons from having the same spin. The Schrödinger equation yields two-electron wave functions for this system which are linear combinations of the individual atomic orbitals (LCAO), where one of the orbitals are symmetric (termed the bonding orbital) and the other is antisymmetric (termed the antibonding orbital). The potential energy of the two atoms is lowered with respect to an isolated atom, due to the contribution from both nuclei and the original isolated energy level splits into two levels; a bonding level with lower energy and antibonding level with higher energy. If many atoms are brought together the split energy levels join together in continuous bands of energies.

As mentioned previously, the energy bands can be separated by energy gaps consisting of forbidden states. For obtaining electrical conductivity, electrons from the valence band must be excited to the conduction band, and the electrons (in CB) and holes in (VB) can move in an electric field. The magnitude of this gap distinguishes metals from semiconductors and semiconductors from insulators. If the conduction band is occupied at absolute zero, i.e. there is no band gap, then the solid is a metal. At 0K all semiconductors are insulators. The main difference between semiconductors and insulators is that as the temperature is increased, the magnitude of the band gap of semiconductors allows electrons from the valence band to be excited to the conduction band. For insulators, the gap between the two bands is too large for excitation under normal circumstances, as seen in figure 2.2.

For some semiconductors (such as ZnO and GaN) the conduction band minimum has the same $\mathbf{k}$ value ($\mathbf{k}$=0) as the valence band maximum. This is called a *direct* band gap because electrons in the VB can be excited to the CB without a change in momentum. An *indirect* band gap occurs if the CB minimum lies at a different $\mathbf{k}$ value than the VB maximum. The

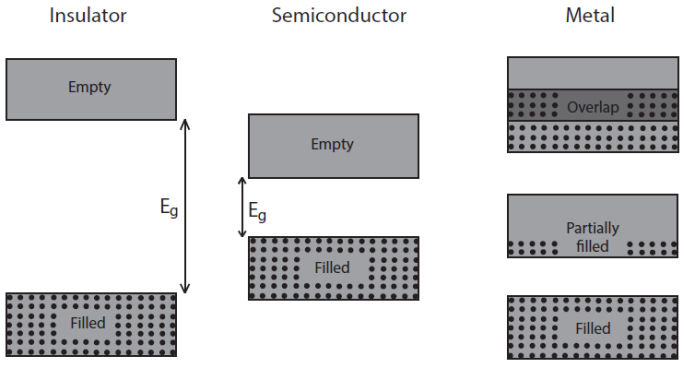

Figure 2.2: *Band structures for insulators, semiconductors and metals at 0K. The main difference between semiconductors and insulators is the magnitude of the band gap. For metals the conduction band can be partially filled or VB and CB can overlap, and electrical conductivity is present at 0K. Figure adapted from Streetman et. al. [6].*

momentum, $\mathbf{p}$, of the plane wave is directly proportional to the wave vector, $\mathbf{k}$, i.e.

$$\mathbf{p} = \hbar\mathbf{k}. \tag{2.6}$$

Hence, for electrons in VB to be excited to CB in an indirect semiconductor, the momentum of the electrons must be changed. This change in momentum is obtained by the contribution of a *phonon*, a quantum of the lattice vibrations.

2.2.2 Intrinsic- and Extrinsic Semiconductors

A perfect semiconductor without dislocations, impurities or other defects is called an *intrinsic semiconductor*. Such a crystal is merely theoretical since it's practically impossible to fabricate. As there are no donors or acceptors in an intrinsic semiconductor, there are no electrons in CB at 0K. At higher temperatures, covalent bonds can be broken by exciting an electron to CB and leaving behind a missing electron in VB, or hole, making an electron-hole pair (EHP). The number of electrons in CB (n) must therefore be equal to the number of holes in VB (p) in an intrinsic material, i.e.

$$n = p = n_i \tag{2.7}$$

where n_i is the number of intrinsic charge carriers.

A semiconductor containing impurities or lattice defects is termed an *extrinsic semiconductor*. The number of charge carriers can be tailored to a specific application by doping of the material. Doping the material is to introduce impurities as either *donors* or *acceptors*. Donors are atoms which have more valence electrons than the semiconductor material. The excess electrons can be donated to the semiconductor and act as conduction electrons. Acceptors on the other hand are atoms with fewer valence electrons, and will therefore accept electrons from the crystal, and hence contribute with holes. Typically the number of introduced impurities are high and the number of electrons (with donor doping) will be so high that the number of holes can be neglected. This is called n-type doping. A p-type semiconductor is doped with a high amount of acceptors and the number of electrons can be neglected.

Donors and acceptors have energy levels termed donor- and acceptor levels respectively, as shown in figure 2.3 (a). If the energy of a donor level is in close proximity to the conduction band, which means that only a small amount of energy is needed to excite the donor electrons to the conduction band, it is called a shallow donor. If the donor level lies closer to the middle of the band gap it is called a deep donor. The same applies to acceptor levels but relative to the valence band. Electrons in VB can easily be excited to these states, leaving behind holes. At 0K any semiconductor, no matter how heavily doped, have no electrons in

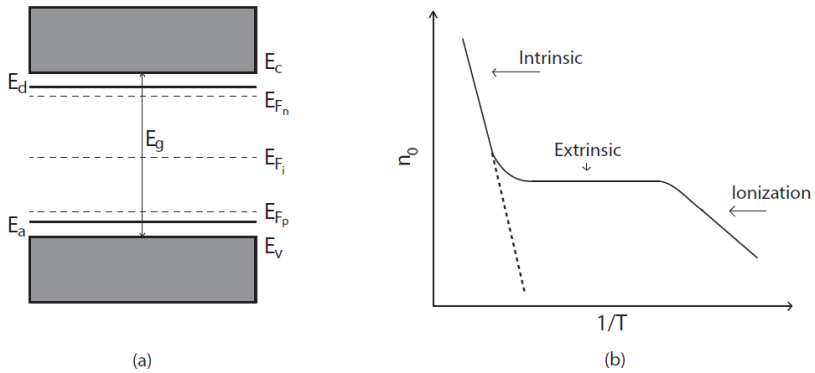

Figure 2.3: *Band gap with donor level, E_d, in close proximity to the conduction band and acceptor level ,E_a, close to the valence band (a). Figure (a) also shows the Fermi level (E_{F_i}) for an intrinsic semiconductor, and the Fermi levels, E_{F_n} and E_{F_p}, for n-type- and p-type semiconductors, respectively. Figure (b) shows the electron concentration in CB as a function of temperature, and which mechanisms dominate. The dashed line shows the same function for an intrinsic semiconductor. Figure adapted from Streetman [6].*

the conduction band. As the temperature is increased for a n-type semiconductor the donor atoms are ionized, i.e. the donor electrons are excited to the conduction band (the ionization part of figure 2.3 b). Further temperature increase leads to all the donor electrons being excited to CB and the increase in electrons excited to CB is zero (the extrinsic region of figure 2.3 b). Finally the temperature is high enough to excite electrons from the valence band to the conduction band (the intrinsic region of figure 2.3 b). The same holds for p-type semiconductors, but then electrons from the valence band are excited to the acceptor levels at relatively low temperatures, leaving holes behind.

2.2.3 Charge carriers in semiconductors

The concentration of electrons in the conduction band has several dependencies. The Fermi-Dirac distribution function gives the probability of an energy state E being occupied by an electron at absolute temperature T;

$$f(E) = \frac{1}{1 + e^{(E-E_F)/kT}} \tag{2.8}$$

while the probability of finding an energy state occupied by a hole is equal to the probability of that energy state **not** being occupied by an electron;

$$1 - f(E) = 1 - [\frac{1}{1 + e^{(E-E_F)/kT}}]. \tag{2.9}$$

E_F is the Fermi level of the semiconductor, k is the Boltzmann constant and T is the temperature. The Fermi level of a semiconductor is the dividing line between occupied and unoccupied states at absolute zero. For intrinsic semiconductors the Fermi level lies in the middle of the band gap, while for extrinsic semiconductors the Fermi level lies closer to the conduction- and valence band for n-type doping and p-type doping, respectively. The distribution function in equation (2.8) is plotted in figure 2.4. From equation (2.8) it is clear that the probability of

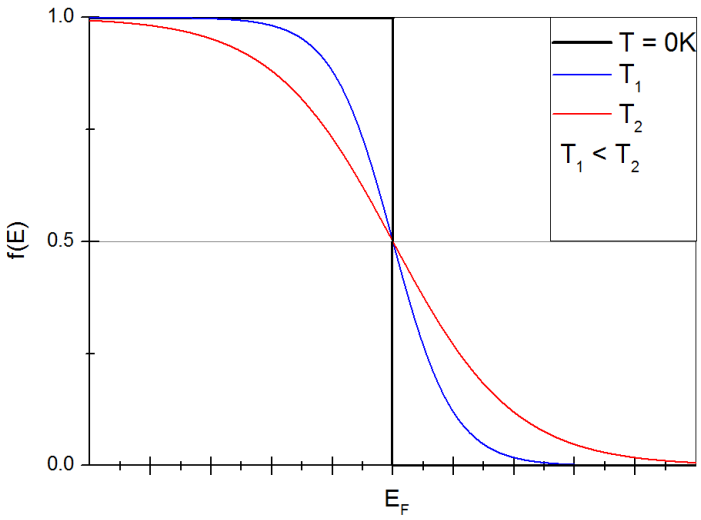

Figure 2.4: *The Fermi-Dirac distribution function. The black line shows the distribution at 0K and the distribution is a step-function at the Fermi energy, whereas for T_1 (blue line) and T_2 (red line) which are temperatures higher than absolute zero, the distributions are more smeared out.*

an energy state E = E_F being occupied is 50% (irrespective of temperature). By examining the probability of the energy state E = E_c being occupied, the concentration of electrons in CB and the hole concentration in VB can be found.

The probability is not the only dependency of the carrier concentration. There must also be available states, termed the density of states N(E). By combining N(E) and the Fermi-Dirac distribution, the respective carrier concentration can be calculated for an energy range dE;

$$n_0 = \int_{E_c}^{\infty} f(E)N(E)dE \tag{2.10}$$

$$p_0 = \int_{0}^{E_v} f(E)N(E)dE \tag{2.11}$$

where n_0 and p_0 are the electron concentrations in CB and hole concentrations in VB at equilibrium, respectively. f(E) is the Fermi-Dirac distribution function and N(E) is the density of states in the energy range dE. The vast majority of electrons are located at the bottom edge of the conduction band. This is because the Fermi-Dirac distribution function becomes very small for large energies, and the probability of finding electrons above the CB minimum decreases exponentially. At low energies, the Fermi-Dirac distribution is close to one and according to equation (2.9) the probability of finding a hole becomes very small. Hence the hole concentration decreases rapidly for energies lower than the top edge of VB. Since most of the electrons in CB are located at the band minimum and the majority of holes in VB

are located at the band maximum, the density of states can be represented by the effective densities of states N_c and N_v for CB and VB, respectively:

$$N_c = 2(\frac{2\pi m_n^* kT}{h^2})^{3/2} \tag{2.12}$$

$$N_v = 2(\frac{2\pi m_p^* kT}{h^2})^{3/2}. \tag{2.13}$$

Where k is the Boltzmann constant, T is the temperature in kelvin, h is the Planck constant and m_n^* and m_n^* is the electron- and hole effective mass, respectively. Since the electrons are mainly located at the CB minimum and the holes at the VB maximum, the Fermi-Dirac distribution function can be adjusted accordingly:

$$f(E_c) = \frac{1}{1 + e^{(E_c - E_F)/kT}} \simeq e^{-(E_c - E_F)/kT} \tag{2.14}$$

$$1 - f(E_v) = 1 - \frac{1}{1 + e^{(E_v - E_F)/kT}} \simeq e^{-(E_F - E_v)/kT}. \tag{2.15}$$

These approximations are allowed if the Fermi level lies several kT below CB and several kT over VB. The number of electrons in the conduction band and the number of holes in the valence band can then be calculated to:

$$n_0 = N_c f(E_c) = N_c e^{-(E_c - E_F)/kT} \tag{2.16}$$

$$p_0 = N_v[1 - f(E_c)] = N_v e^{-(E_F - E_v)/kT}. \tag{2.17}$$

These expressions for charge carriers can be used for both intrinsic and doped semiconductors as long as they are in thermal equilibrium. For an intrinsic semiconductor the Fermi level lies at the middle of the band gap:

$$n_i = N_c e^{-(E_c - E_i)/kT} \tag{2.18}$$

$$p_i = N_v e^{-(E_i - E_v)/kT}. \tag{2.19}$$

Where E_i is the intrinsic Fermi level in the middle of the band gap. For a semiconductor in thermal equilibrium the product of electrons in CB and holes in VB is constant (regardless of doping), and the product of equations (2.16) and (2.17) is constant and equal to the product of equations (2.18 and 2.19). This gives the important relation:

$$n_0 p_0 = n_i p_i = N_c N_v e^{-E_g/kT} \tag{2.20}$$

$$n_0 p_0 = n_i^2 \tag{2.21}$$

and the concentration of electrons in CB and holes in VB can be expressed by the intrinsic carrier concentration:

$$n_0 = n_i e^{(E_F - E_i)/kT} \tag{2.22}$$

$$p_0 = n_i e^{(E_i - E_F)/kT} \tag{2.23}$$

where the intrinsic carrier concentration, n_i, is given by:

$$n_i = \sqrt{N_c N_v} e^{-E_g/2kT}. \tag{2.24}$$

For a semiconductor, the requirement of space charge neutrality must be obeyed. For an intrinsic semiconductor, the neutrality is fulfilled due to the definition of an intrinsic semiconductor, i.e. the number of electrons in CB and holes in VB are equal ($n_0 = p_0$). An extrinsic semiconductor containing donors, acceptors or both, the space charge neutrality is obeyed by;

$$p_0 + N_d^+ = n_0 + N_a^- \tag{2.25}$$

Where p_0 and n_0 is the hole- and electron concentrations, and N_d^+ and N_a^- is the number of ionized donor- and acceptor atoms, respectively. The carrier concentration in an extrinsic semiconductor can conveniently be expressed by the doping; for n-type semiconductors with N_d donors at room temperature, the number of electrons in the conduction band can be approximated to the number of donors. The number of holes in the valence band can then be obtained by utilizing equation (2.21):

$$n_0 \approx N_d \tag{2.26}$$

$$p_0 \approx \frac{n_i^2}{N_d} \tag{2.27}$$

This approximation is valid in an n-type semiconductor, since the number of donors is several orders of magnitude larger than the number of intrinsic carriers. By the same argument the hole concentration in the valence band, and the electron concentration in the conduction band of a p-type doped semiconductor is given by:

$$p_0 \approx N_a \tag{2.28}$$

$$n_0 \approx \frac{n_i^2}{N_a} \tag{2.29}$$

2.3 Epitaxial growth of semiconductor thin films

This section is based on the textbooks of Venables [12] and Campbell [13]. A thin film is grown epitaxially on a surface, if the film uses the substrate's crystal structure as a template. If the substrate and the film are two different materials the growth is called *heteroepitaxial*, while if they are the same the growth is referred to as *homoepitaxial*. Commonly, three types of growth modes are referred to when discussing epitaxial growth. The first growth mode is called the *Frank-van der Merwe* mode, and is a layer-by-layer mode. The Frank-van der Merwe mode occurs when the deposited adatoms are more attracted to each other than the substrate, hence resulting in a layer covering the substrate. *Volmer-Weber* is the second mode of growth and is commonly referred to as island growth since the resulting film consist of tree-dimensional islands, or grains. Island growth occurs when deposited adatoms are more attracted to the substrate that they are to themselves. The third growth mode is called *Stranski-Krastanov*, and is a layer-plus-island growth mode. A layer is made by the adatoms covering the surface, before islands starts forming. The Volmer-Weber- and Stranski-Krastanov growth modes are referred to as 3D-growth. The Stranski-Krastanov mode is the most common growth mode in semiconductor thin film processing.

The two-dimensional Frank-van der Merwe growth is often explained by the terrace-kink model. If the substrate surface consists of two or more terraces, the adatoms on the lower terrace will diffuse to the edge between the two terraces and the top terrace will expand over the lower terrace. These terraces or steps can be produced intentionally by cutting the

substrate at an angle, so that the surface normal deviates slightly from a major axis. Steps can also be present due to dislocations, such as screw dislocations. If the rate of deposited atoms or molecules is too high, or if the adatom surface mobility is too low, island (3D) growth will proceed.

2.4 Zinc Oxide

2.4.1 Crystal structure

ZnO is a II-VI semiconductor, with wurtzite as the thermodynamically stable phase at ambient conditions. ZnO has a hexagonal unit cell with the lattice parameters
a = b = 3.2495 (± 0.00002) Å and c = 5.2069 (± 0.0001) Å as determined by Heller et. al. [14], and belongs to the space group $P6_3mc$ as seen in figure 2.5. The structure consists of alternating biatomic (0001) planes with a stacking sequence of AaBbAaBb$\cdots$ in the $\langle 0001 \rangle$ direction [15]. The two interpenetrating sublattices of the wurtzite structure are hexagonal-close-packed (hcp). This means that each Zn atom is surrounded by four oxygen atoms placed at the edges of a tetrahedron and vice versa. These tetrahedrons are generally of sp^3 covalent bonding, but the II-VI semiconductors ionicity makes the bondings a combination of ionic and covalent. ZnO has a six-fold symmetry about the c-axis, and its wurtzite structure has no inversion symmetry, i.e. the (0001) plane is different from the $(000\bar{1})$ plane, which means that the crystal exhibits crystallographic polarity.

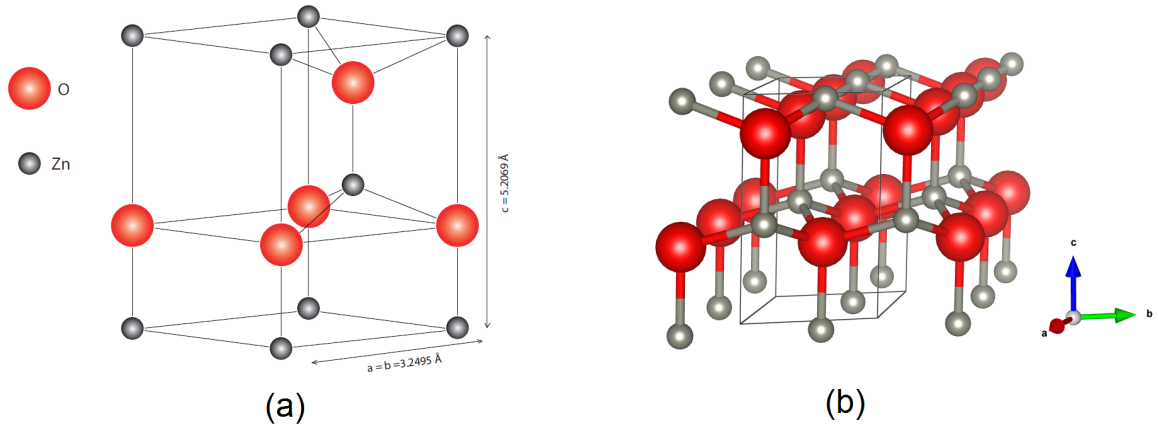

Figure 2.5: *Illustration of wurtzite ZnO in its hexagonal unit cell (a) and more atoms added to illustrate the alternating biatomic planes (b). The cell parameters are a = b = 3.2495 Å and c = 5.2069 Å. Figure (b) was created using the VESTA software [16].*

The positive z direction for the crystal is the [0001] axis which points from the face of the oxygen plane to the zinc plane. Bonds along the c direction going from an zinc cation to an oxygen anion has a Zn polarity, and the opposite is true for bondings from oxygen to zinc and the two sides of the crystal is called Zn-face [0001] and O-face $[000\bar{1}]$.

2.4.2 Electronic properties and defects

Zinc oxide has a direct wide band gap ($E_g \sim 3.3$ eV at 300 K) [15]. The top of the valence band is formed from the oxygen 2p levels, while the bottom of the conduction band is formed mainly from the Zn 4s levels [17]. Zinc oxide is commonly *n*-type while *p*-type behavior has proved to be extremely hard to achieve. In every semiconductor there will be defects and unintentionally incorporated impurities, and in ZnO the most common defects are zinc and oxygen vacancies (V_{Zn} and V_O respectively), since the formation energy for V_{Zn} and V_O are lowest for O-rich and Zn-rich conditions, respectively [15, 18]. Zinc vacancies, which are dominant for oxygen-rich conditions, have charge -2 in *n*-type ZnO. The transition level between the -1 and -2 charge states of the zinc vacancy occurs at $\sim$ 0.8 eV above the valence band, making the vacancy a deep acceptor [15]. In his paper Van de Walle [19] determined that oxygen vacancies are deep donors in ZnO and the transition from the +2 state to the neutral state occurs $\sim$ 2.7 eV above the valence band. However the +2 state of V_O is unstable and is hence not expected to be observable. Oxygen vacancies are dominant under Zn-rich conditions. Zinc interstitials (Zn_i) are also likely to form, but Zn_i has a higher formation energy than V_O and hence the oxygen vacancies are dominant. Hydrogen is a common impurity in semiconductors because incorporation during growth is nearly impossible to avoid [20]. In common semiconductors hydrogen acts as a donor (H^+) in *p*-type materials and an acceptor (H^-) in *n*-type materials, whereas in ZnO hydrogen always acts as a donor [21].

2.4.3 P-type ZnO

P-type ZnO has proved to be very hard to obtain since introduced acceptors are compensated by native defects as zinc interstitials and oxygen vacancies [22]. ZnO has a natural n-type behavior, due to deviations in stoichiometry resulting from native defects such as oxygen vacancies and zinc interstitials [15] or from unintentional donor doping. To obtain p-type behavior, the n-type material must then be compensated, i.e. introduce acceptors to make the material intrinsic ($n_0 = p_0$) [6]. By introducing even more acceptors, hole conduction will become dominant and the material is p-type. Theoretically, by substituting zinc with group-I elements or substituting oxygen with group-V elements, p-type conduction could be obtained [15]. Possible group-I elements for obtaining p-type behavior in ZnO are Li, Na and K. These dopants, if placed on Zn-sites will contribute to p-type behavior as shallow acceptors. However, p-type doping with group-I elements are found to be limited by group-I elements forming compensating interstitial donors [23]. One of the most promising dopant for obtaining p-type behavior in ZnO is nitrogen, N. Nitrogen substituting for oxygen sites forms shallow acceptors [23]. Lee et. al. [24] found that when incorporating nitrogen in ZnO, other N-related donor defects also form, such as $(N_2)_O$ and N_O-double-donor complexes. More recently, the codoping method was suggested to give more positive results; Li et.al. [3] fabricated ZnO films codoped with Ag and N, where depending on annealing time, the films showed p-type conduction. The p-type behavior was relatively stable, but the resistance increased and carrier concentration decreased with time. Ag substitutes for Zn and acts as an acceptor, but the p-type conductivity was reported to be attributed to [Ag-N]-related acceptor complexes, such as the Ag_{Zn}-N_O pairs and N_O-Ag_{Zn}-N_O triangles. Xu et. al. [4] also obtained p-type behavior for ZnO thin films using codoping. Ag-S codoping resulted in Ag substituting for Zn and S substituting for O, making Ag_{Zn}-S_O complexes that acts as acceptors.

2.4.4 ZnO as LED

A *light emitting diode* (LED) is a pn-junction[1] where the current is injected in forward bias. Whereas in a solar cell photons excite carriers, which can contribute to the current, the LED operates oppositely. Current is passed through the device in forward bias, and e^--h^+ recombinations occur within the neutral (depletion) region of the pn-junction. When excited electrons and holes recombine in a direct band gap semiconductor, the energy is released by emitting photons. The emitted light will have the color corresponding to the band gap energy [6].

Since electrons and holes form tightly bound excitons in ZnO, near-band-gap recombinations are efficient at room temperature, and ZnO is highly suited for LED devices [23]. P-type ZnO were fabricated and violet electroluminescence from homostructural p-i-n junctions were demonstrated by Tsukazaki et. al. [25]. The report involved nitrogen doped p-type ZnO thin films and junction devices grown by laser MBE. The p-ZnO had a hole concentration of 2×10^{16} cm^{-3}, and i-ZnO and n-ZnO had electron concentrations of 2×10^{16} cm^{-3} and 2×10^{19} cm^{-3}, respectively. The electroluminescence spectrum showed luminescence from violet to green regions with multi-reflection interference fringes. Chu et. al. [26] reported a UV LED with a ZnO p-n homojunction. The homojunction was grown on a Si (100) substrate with MgO/ZnO as a buffer layer between the substrate and the homojunction. The n-type ZnO was doped with Ga, while the p-type ZnO was Sb-doped. The hole concentration in the p-layer was lower than the electron concentration in the n-layer, and hence the depletion region was mainly in the p-region. The diode showed good UV emissions at different temperatures.

2.4.5 ZnO as TCO

A *transparent conductive oxide* (TCO) can act as the top electrode of a solar cell. For a TCO to be efficient as an electrode (front and back), the material must posses some crucial properties; the resistivity should be as low as possible, meanwhile the carrier concentration is reduced to reduce unwanted free carrier absorption in the infra-red range. The mobility of the carriers on the other hand should be as large as possible, to increase the TCOs conductivity, while at the same time keeping the absorption coefficient low [27]. Park et. al. [28] deposited Ga-doped ZnO on quartz substrates using pulsed laser deposition. A resistivity of 8.12×10^{-5} Ωcm and a visible transmittance of above 90% was obtained for sample deposited at 300°C. Chen et. al. [29] used pulsed direct current (DC) magnetron sputtering to grow ZnO thin films co-doped with Mg and Ga, with variation of the H_2 gas flow, for TCO applications. They found that Mg-doped ZnO (MGZO) deposited on glass, with a H_2 flow rate ratio of 4/59 sccm and the remaining 55sccm Ar, yield the thin films with lowest resistivity (1.96×10^{-3} Ωcm) and with an average transmittance of 80.5% in the wavelength range from 340 nm to 1100 nm. The hydrogen flow rate was also varied in the work of Tian et. al. [30]. In this work, TCO ZnO thin films were grown and co-doped with Mg and Ga by using magnetron sputtering. The hydrogenated Mg and Ga co-doped ZnO (HMGZO) thin film grown with a

[1] A pn-junction is a p-type material brought together with an n-type material. The electrons on the n-side and holes on the p-side will then diffuse to the opposite side, leaving behind uncompensated donors and acceptors, respectively. As more carriers diffuse, an electric field will be built up in the transition (depletion) region, preventing further diffusion. Band bending occurs in order to keep the Fermi level constant throughout the device, and the potential difference between the n- and p-side is called the contact potential. When the junction is in equilibrium, the carrier diffusion due to the concentration gradient and the carrier drift due to the electrical field in the transition region cancel each other out, resulting in no net current [6].

H_2 flow rate ratio 9/64 sccm and the remaining 55 sccm Ar, gave a resistivity of 4.4×10^{-3} Ωcm. The average transmittance was 88.6% in the wavelength range from 330 nm to 1100 nm.

2.5 Previous work

Due to the higher deposition rates possible for sputtering and the possibility of large-area deposition compared to metalorganic chemical vapor deposition (MOCVD) and molecular beam epitaxy (MBE), the potential homoepitaxial growth of ZnO by sputtering would be a step towards upscaling. Kim et.al. [31] reported homoepitaxial growth by sputter deposition at 75W and 800 ^{0}C. Thin films were grown on commercial wafers obtained from three different manufacturers (CrysTec, MTI and Mahk). Characterization was done using X-ray diffraction and Photoluminescence spectroscopy. Full width at half maximum for XRD rocking curve scan was found to be 10 arcsec - 65 arcsec and the FWHM for the band edge PL peak was found to be 106 meV. They also found that growth on Zn-face substrates gave higher crystal quality, with lower defect concentrations than growth on O-faced substrate. Furusawa et. al. [32] reported homoepitaxial ZnO film using helicon-wave-excited-plasma sputtering epitaxy (HWPSE), to reduce the surface damage during deposition. Atomically-flat ZnO epitaxial films were grown on Zn-polar (0001) ZnO substrates with a miscut of 0.05^0 and 0.08^0 in the *m*- and *a* axes respectively, by using a polycrystalline ZnO target. Substrates were purchased from Tokyo Denpa. A varying mixture of O_2 and Ar gas was used with RF power varied from 200 to 320W and temperatures between 950 and 970 ^{0}C. A Step-and-terrace surface structure with a monolayer height of 0.26 nm and a RMS roughness of 0.1 nm was achieved. The photoluminescence spectra showed a near-band exciton emission peak at 3.267eV, with a FWHM of 65 meV.

Deposition of ZnO thin films on ZnO substrates can yield different results depending on the polarity of the substrate surface. Zhu et. al. [33] annealed ZnO substrates with temperatures varying from 200 to 800^0C in air for 1-20h before deposition. Films were grown by off-axis RF magnetron sputter deposition with a total pressure of 50 mTorr and temperature of 550^0C. They found that O-faced substrates are better for film growth as it was found that high temperature annealing improves the O-faced substrates, while for the Zn-faced substrates no major effects of annealing was found.

Chapter 3

Experimental Methods

3.1 Sputtering

This section is based on the textbooks of Campbell [13], Ellmer [34] and Chapman [35]. Sputtering is a technique used for thin film deposition. In the technique an inert gas is introduced between two electrodes in a low pressure chamber. A target material is placed at the cathode, while the shield covering the rest of the target holder placed 3 mm from the cathode is the anode. The substrate is placed on a substrate holder that is electrically isolated from the rest of the chamber which is grounded. A voltage difference between these two electrodes ionizes the gas, resulting in plasma formation. Once the plasma is formed, the voltage between the two electrodes accelerates the positively charged gas ions towards the negatively charged cathode; the ions will eject target material which will travel through the chamber and be deposited on the substrate surface.

Magnetron sputtering is a related technique which utilizes electric and magnetic fields to confine the plasma in front of the target material. Magnetic force is defined as:

$$\overrightarrow{F} = q\overrightarrow{v} \times \overrightarrow{B} \tag{3.1}$$

where q is the particles charge, $\overrightarrow{v}$ is the velocity vector of the particle and $\overrightarrow{B}$ is the magnetic field vector. The force bends the electrically charged particles in a circular path in the direction perpendicular to the magnetic field and the velocity of the particle. The radius of the circular motion is given by:

$$r = \frac{mv}{qB} \tag{3.2}$$

where B is the magnetic field and m, v and q are the particles mass, velocity and charge, respectively. From this it is easily seen that the influence of the magnetic field on the particle depends on its mass. The strength of the magnetic field is hence adjusted so that the electrons get a cylindrical motion through the magnetic and electric fields, leading to a high ionization efficiency. The heavy ions on the other hand will only be negligibly influenced by the magnetic field.

In comparison to other deposition methods magnetron sputtering has several advantages. It allows for deposition at low substrate temperature, provides high deposition rates, good

thickness uniformity and good adhesion of films on substrates.

3.1.1 Plasma

A plasma is a partially ionized gas. The typical gas injected in the sputter chamber is Ar. When the gas ions are bombarded onto the target surface, they will generate secondary electrons in addition to ejecting target material. These secondary electrons are then accelerated towards the positive charged anode, and collisions with neutral gas atoms will result in more positively charged ions. In this way the plasma is maintained. When high energy ions strike the surface of the target, different processes can happen depending on the energy of the ions. If the energy of the incoming ions is appropriate, surface atoms and molecules can be ejected from the target material towards the substrate. If the ion energies are too high the result would be implantation instead of sputtering, while if it is too low the ions would be either reflected or adsorbed.

The electrons are quickly accelerated away from the cathode, which means that the electron density near the cathode is small compared to the ion density. Hence this area has a net positive charge which shields the plasma from the charge on the cathode. This is shown in figure 3.1. The region right in front of the cathode is termed Crookes dark space. A dark

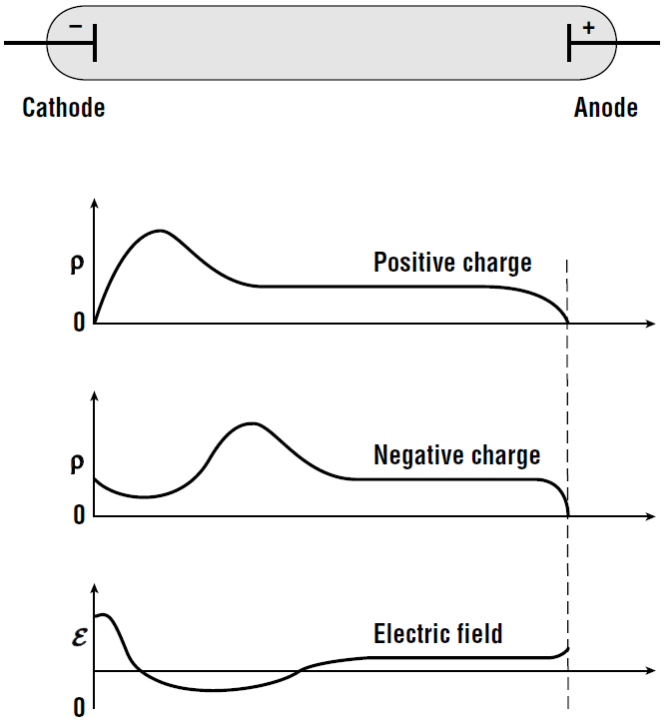

Figure 3.1: *Positive and negative charge densities, as well as electric field, as a function of position in the plasma. The figure is adapted from Campbell [13].*

space is an area which precludes optical emission. This emission comes from electrons which

have a too low energy to ionize neutral gas atoms, and instead excite a core level electron in the gas atoms .

3.1.2 RF Sputtering

For deposition of insulating materials, or materials with very low conductivity, a radio frequency (RF) voltage source is required. If the material is insulating, the ejection of secondary electrons will build up a surface charge, which will eventually extinguish the plasma. RF sputtering therefore uses an ac signal at RF to keep the plasma going. This alternating voltage leads to the target material being bombarded by ions and electrons alternately resulting in no build up charge on the surface.

3.1.3 Sputter yield, deposition rate and thin film properties

The sputter yield is an important parameter affecting the deposition rate. The sputter yield, S, is defined as the number of sputtered target atoms per incident ion:

$$S = Z_e/Z_i. \tag{3.3}$$

Here Z_e is the number of ejected target atoms and Z_i is the number of incident ions. Although the sputter yield has a great influence on the deposition rate, it is not the only factor affecting it. The rate also depends on the ion flux to the target and the transport of sputtered material across the plasma. The mobility of the target atoms on the substrate surface depends on the kinetic energy of the atoms when they hit the surface, in addition to the surface temperature and the binding energy between the sputtered atoms and the substrate species. High kinetic energies give the atoms a high surface mobility and a higher probability of finding an energetically favorable place on the surface. With sufficient surface mobility, atoms will diffuse on the surface to form islands. As more atoms are sputtered on to the surface, these islands will grow and eventually form smooth and uniform thin films. If both the ion energy and the temperature is low, the adatom mobility will be low resulting in an amorphous film with a low mass density. Small grains, which are desired in microelectronics are obtained by raising the temperature or lowering the pressure. On the other hand, if the temperature and/or ion energy is higher, the grain size becomes larger. Larger grains are desired in TCO applications, because of higher transmittance and mobility.

3.2 X-Ray Diffraction

This section is based on the textbook by Birkholz [36]. X-ray diffraction (XRD) is a method used to analyze the structural properties of crystalline materials. When x-rays are incident on a sample, scattering events will occur. By measuring the angle and intensity of the output radiation with respect to the incident, the structural properties of a sample can be determined. Three different interactions between x-rays and matter are relevant; photoionization and Compton scattering which are inelastic scattering processes which excite electrons and Thomson scattering. In Compton scattering the electrons are not released from the atom,

while in photoionization the incoming radiation ionizes the atom. In Thomson scattering x-rays are scattered elastically by electrons oscillating like a Hertz dipole at the frequency of the incoming beam and the oscillating electrons then become a source of dipole radiation. The incoming beam can be described as a plane wave $\mathbf{E}_0\exp(-i\mathbf{K}_0\mathbf{R}_0)$. $\mathbf{R}_0$ is the position of the single free electron in the elastic scattering process, $\mathbf{E}_0$ is the electrical field while $\mathbf{K}_0$ describe the direction of the incident beam. The direction of the outgoing beam is described by $\mathbf{K}$. The angle between $\mathbf{K}$ and the prolonged direction of $\mathbf{K}_0$ is defined as 2θ, also referred to as the scattering angle;

$$2\theta = arccos\frac{\langle \mathbf{K}, \mathbf{K_0} \rangle}{KK_0} \tag{3.4}$$

Where K and K_0 are the magnitudes of the $\mathbf{K}$ and $\mathbf{K}_0$ vectors, respectively. The vector difference $\mathbf{K}$-$\mathbf{K}_0$ is called the scattering vector, Q, and is defined as;

$$\mathbf{Q} = \mathbf{K} - \mathbf{K_0} \tag{3.5}$$

The physical meaning of the scattering vector in a mechanical analogy is that of momentum transfer. $\mathbf{Q}$ is therefore also called the vector of momentum transfer. The direction of momentum transfer is given by $\mathbf{p}$-$\mathbf{p}_0$, while the strength is given by $|\mathbf{p}$-$\mathbf{p}_0|$. Since the scattering vector is defined as the difference between the incident beam vector and the outgoing beam vector, the orientation of these determine the direction of momentum transfer. For a simple cubic system the highest scattered intensity is achieved when:

$$\begin{aligned} a\mathbf{Qc_1} &= 2\pi h \\ a\mathbf{Qc_2} &= 2\pi k \\ a\mathbf{Qc_3} &= 2\pi l \end{aligned} \tag{3.6}$$

The $\mathbf{c}_j$ vectors are the unit vectors of the three orthogonal directions in space, a is the lattice constant and h,k,l are the Miller indices.

The set of conditions in equation (3.6) is called the Laue conditions. By multiplying the conditions in equation (3.6) by the inverse cell parameter 1/a, adding the squares and taking the square root, the condition for maximum intensity becomes:

$$\frac{|\mathbf{Q}|}{2\pi} = \frac{\sqrt{h^2+k^2+l^2}}{a} \tag{3.7}$$

Using the fact that the magnitude of the scattering vector is

$$|\mathbf{Q}| = \frac{4\pi sin(\theta)}{\lambda} \tag{3.8}$$

the relation between the wavelength of the incoming x-ray (λ), the scattering angle (θ) and the crystal properties (represented by the Miller indices) is obtained:

$$\lambda = 2\frac{a}{\sqrt{h^2+k^2+l^2}}sin(\theta) \tag{3.9}$$

Since the distance between two adjacent planes d_{hkl} for a cubic lattice is given by:

$$d_{hkl} = \frac{a}{\sqrt{h^2+k^2+l^2}} \tag{3.10}$$

equation (3.9) can be written:

$$2d_{hkl}sin\theta_B = \lambda \tag{3.11}$$

This is the Bragg relation, where θ_B is the Bragg angle which is the position of maximum reflected x-ray intensity. When an x-ray plane wave is scattered from an atom plane in a crystal with a spacing of d_{hkl} between the planes, the phase shift of the wave is 2dsinθ for any angle θ. However constructive interference can only be achieved when the phase shift is equal to a multiple ,n, of the wavelength, i.e.:

$$2dsin\theta_B = n\lambda \tag{3.12}$$

where n is a integer. This can be understood by viewing figure 3.2. Although the simple cubic

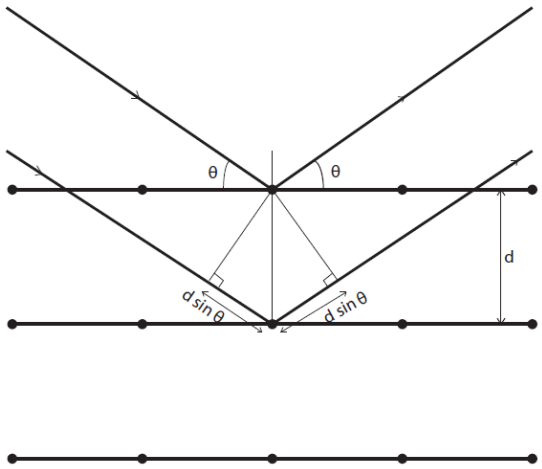

Figure 3.2: *The Bragg relation can be used to evaluate the interplanar spacing d. The plane wave which hits the second crystal plane, has to travel a distance 2dsinθ longer than the wave scattered by the first plane.*

crystal system has been the example throughout this derivation, the Bragg relation is valid for other crystal systems as well.

3.2.1 $\theta/2\theta$ Scan

As stated by now, Bragg reflections are of major interest for thin films characterization by x-ray diffraction. Their position, shape and intensity are important to determine the crystal properties of the film.

The setup for a $\theta/2\theta$ scan is shown in figure 3.3. Since the scattered intensity depends on the distance between the sample and detector, the detector is moved on a constant radius hemisphere around the sample. Any intensity variations is thus due to beam-sample interactions. During the scan, the angle of the incoming beam and detector angle with respect to the sample is varied, but kept equal to each other, i.e. $\theta_{in} = \theta_{det}$, with maximum intensity occuring when equation (3.12) is fulfilled. The width of a Bragg reflection peak contains information about the crystallite size and distortion of the crystal structure such as microstrain

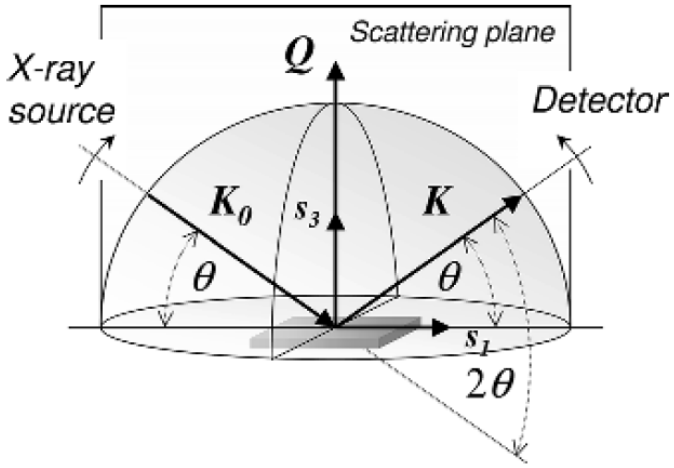

Figure 3.3: *A sketch of the instrumental setup for a $\theta/2\theta$ scan. The detector moves with a constant radius from the sample to ensure that any variations in intensity is due to beam-sample interactions. The angle θ is varied, but θ_{in} and θ_{det} is kept equal. Figure adapted from Birkholz [36].*

and dislocations. Dislocations cause strain in a material. Due to this strain, the observed interplanar spacing d may be a distribution of d values. A wide Bragg reflection peak can thus be understood as a distribution of the interplanar spacing d, but also the size of coherently scattering domains contributes.

An important parameter when analyzing a Bragg reflection peak is the full width at half maximum (FWHM), which is defined as $2w$. With the FWHM, the peak position $2\theta_0$, and the peak intensity at the centroid I_0, one can use the Cauchy function, the Gauss function or a combination of the two to analytically fit the peak. The Cauchy function is associated with small crystallite size, whereas the Gauss function is associated with microstrain in the crystal. The Cauchy and Gauss functions, f_C and f_G respectively, are given by the formulas in equation 3.13:

$$\begin{aligned} f_C &= [1 + (2\theta - 2\theta_0)^2/w^2]^{-1} \\ f_G &= exp[-ln2(2\theta - 2\theta_0)^2/w^2] \end{aligned} \tag{3.13}$$

By multiplying these functions with the intensity at the centroid I_0, the Bragg reflection profile can be approximated.

The position of Bragg reflection peaks is material dependent, so by comparing experimental results with literature the chemical composition of a material can be obtained. Strain and stress in the film can also be calculated using the $\theta/2\theta$ scan. By using the θ value for the peak, the interplanar spacing can be calculated according to Bragg's law (3.11). Cebulla et. al. [37] found that the strain in the film perpendicular to the substrate surface was given by

$$\epsilon = \frac{c_{film} - c_{bulk}}{c_{bulk}} \tag{3.14}$$

where the values c_{film} and c_{bulk} are the measured and theoretical values of the c lattice constant for the ZnO unit cell, respectively. The stress parallel to the substrate surface could be calculated using the elastic constants c_{ij};

$$\sigma_{film} = \frac{2c_{13}^2 - c_{33}(c_{11} + c_{12})}{2c_{13}} \times \epsilon = -233\epsilon. \tag{3.15}$$

The stress in the film is given in GPa.

3.2.2 Rocking Curve Scan

The rocking curve scan is commonly used to analyze thin film crystal planes parallel to a sample surface. In the scan mode the 2θ angle is kept constant at a Bragg peak, while the sample is tilted. Tilting the sample means that θ and 2θ are no longer locked together as in the $\theta/2\theta$ scan and the rocking curve scan is hence called a decoupled scan mode. The sample tilt is described by ω, where ω relates to the surface normal ($\mathbf{s}_3$ in figure 3.4) and is defined as;

$$\omega = \theta - 2\theta_0/2 \tag{3.16}$$

which is the deviation from half the scattering angle of the symmetric position, as shown in figure 3.4. Since the 2θ angle is kept constant at a specific Bragg reflection and the sample

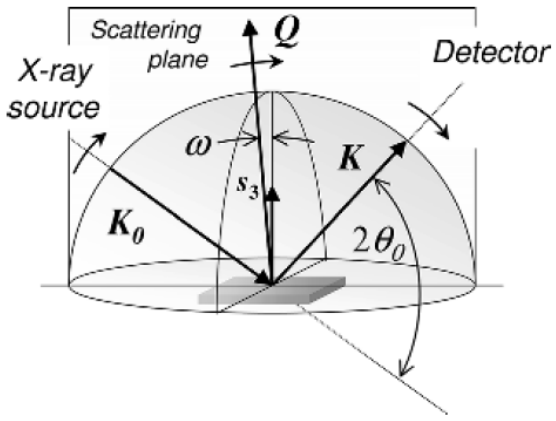

Figure 3.4: *A sketch of the instrumental setup for a rocking curve scan. The 2θ angle is kept constant at a Bragg peak, while the sample is tilted. The tilt is described by ω. Figure adapted form Birkholz [36]*

is tilted about the ω axis, the rocking curve scan gives an intensity plot as a function of ω. The intensity plot of an ideal rocking curve scan will have the shape of a Gaussian curve. Rocking curve scan can detect different dislocations within the thin film. Edge dislocations produce distortion within lattice planes parallel to the surface, but do not disturb the position of these planes in the layer normal direction [38]. This distortion in lattice planes results in a broadening in the rocking curve intensity plot. Another reason for the peak broadening can be screw dislocations in the film. These dislocations result in a tilt of lattice planes [39]. A wide rocking curve peak can be interpreted as the presence of several different tilted crystal planes (e.g. originating from dislocations), whereas a side-peak could indicate a slight tilt in the thin film compared to the substrate if these have the same crystal symmetry.

3.2.3 ϕ Scan

Another orientational degree of freedom of interest is the rotational twist about the c-axis. Crystallite rotation in the a,b-plane is examined in a ϕ scan where the source and detector (θ and 2θ) are held fixed at a Bragg peak, while the sample holder is rotated around the ϕ-axis. The ϕ scan can thus be used to analyze the distribution of in-plane orientations and the epitaxial relationship between the thin film- and the substrate axes in the plane [40].

3.3 Atomic Force Microscopy

This section is based on the textbooks by Mironov [41] and Leng [42]. Atomic force microscopy (AFM) is a widely used method for characterization of material surfaces based on the interaction between the surface atoms and the tip of an elastic cantilever. Four types of forces are critical to understand the mechanisms of AFM. At large distances dipole-dipole interactions cause attraction between the tip and the surface, while for distances smaller than the atomic spacing (a few Å), short-range forces cause a repulsive interaction. In addition, a difference in electric potential between the surface and the tip gives rise to long-range electrostatic forces. As measurements are commonly done in air, capillary forces must also be taken into account. These forces result from water vapor condensing between the tip and the surface, and are the strongest of the forces discussed here.

As a tip is swept over the surface of a sample, the forces between the tip and the surface will result in bending of the cantilever. The deflections are recorded by focusing a laser on the cantilever, which reflects the beam on to a position-sensitive photo detector. Any movement of the cantilever in either the normal- or lateral directions will be picked up by the detector, and an accurate description of the surface topography can be recorded. The distance between the photo diodes and the cantilever is about three orders of magnitude larger than the size of the cantilever, which magnifies the tip movements and hence gives extremely high sensitivity.

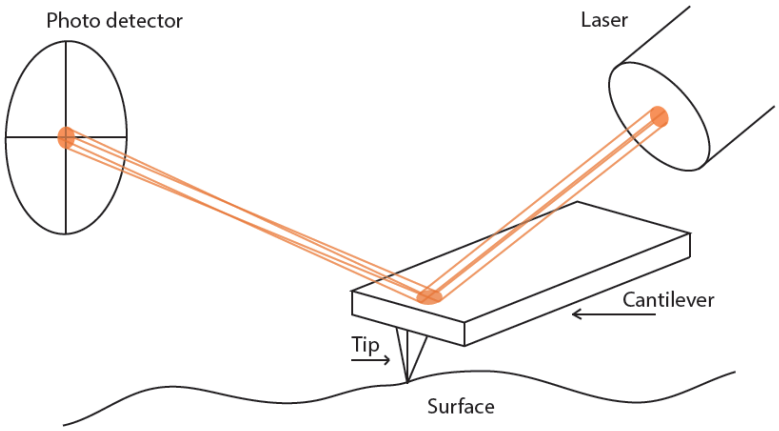

Figure 3.5: *Illustration of the experimental setup of an atomic force microscope measurement. The laser beam is focused on the cantilever and reflected to the photo diode. As the tip scans the surface, movement in the normal- or lateral directions will be detected by the photo diode.*

3.3.1 Tapping mode

Two different operational modes are available in an atomic force microscope, namely static- and dynamic mode. The dynamic mode is based on the cantilever oscillating at a fixed frequency, trying to maintain a certain amplitude during the scan. Different dynamic modes exist, but the most widely used is tapping mode. Tapping mode is a so-called semi-contact mode. The cantilever is oscillated at its resonant frequency, and during the measurement, the tip will lightly touch the surface during the lower part of the oscillation and the change in phase and amplitude is recorded. The cantilever is kept at a constant frequency, and when the tip is scanned over an elevation on the surface, the cantilever has less room to oscillate and the amplitude decreases, while the reverse case is true when the tip is scanned over a depression. The phase change of the cantilever oscillations is very sensitive to material composition and is not effected by large height differences, and makes tapping mode highly suited for imaging grain boundaries since these can be obscured by rough topography. A further advantage of using tapping mode is its gentle tip-surface interaction, preventing scratches and damage to the surface.

3.3.2 Resolution and noise

Atomic force microscopy is a relatively simple imaging technology that yields a high resolution. To achieve optimum resolution, several factors must be taken into consideration. The tip of the cantilever has several properties such as size and shape which affect a measurement. For smooth surfaces with small depressions and elevations, the tip should be as small and thin as possible. If the tip is wide, a broadening of hills and a narrowing of depressions on the surface will appear. Vibrations reduce the resolution of an image as floor and acoustic vibrations can make oscillating patterns in an AFM image. Certain procedures are available to minimize these errors, such as making several scans, scanning in different directions and changing the scan speed.

3.3.3 Tuning fork sensor

This subsection is based on the articles by Giessibl [43], Giessibl et. al. [44] and Albrecht et. al [45]. A tuning fork sensor can be used in AFM. The fork is mounted with the base part fixed and the prongs oscillating opposite to each other, perpendicular to a sample surface normal. The tip is attached to the prong closest to the sample surface, while something of equal mass is attached to the other prong to obtain the same resonant frequency.

The sensor is operated in a frequency modulation mode, meaning the prongs serves as the frequency-determining element of a constant amplitude oscillator, and any change in force gradient acting on the tip will hence change the oscillation frequency of the fork. As the height difference between the sample surface and the tip deviates from the set-point due to elevations or depressions, the oscillation frequency changes. The frequency variations are calculated and the sensor is lifted or lowered to restore the initial frequency, and this change in height is recorded and converted to a topography image.

3.4 Rutherford Backscattering Spectroscopy

This section is based on Palmetshofer [46] and Bakhru [47]. Rutherford Backscattering Spectroscopy (RBS) is a very simple and non destructive method for thin film analysis. A beam of monoenergetic ions is accelerated towards a sample, and detection of the backscattered ions (seen in figure 3.6) provides information on thickness, depth profiles, composition and crystal quality. The monoenergetic ions used in RBS are usually H^+ or He^+ with an energy range of 0.5 to 2.5 MeV. The ions collide with the atoms, resulting in large-angle scattering events called backscattering. The backscattered ion‘s energy is then detected. The incident ions also lose energy ionizing and exciting the sample atoms, leading to a broadened peak in the RBS spectrum. Ions backscattered from heavy elements will have higher energies than those backscattered from lighter elemtents.

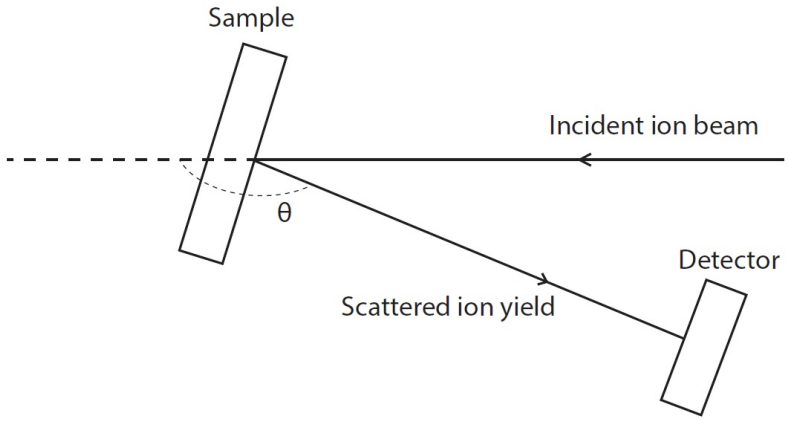

Figure 3.6: *The experimental setup of a RBS measurement. The angle θ is the scattering angle.*

RBS is commonly used to analyze the crystal quality of materials, in a mode termed channeling (RBS/C). When the incident ion velocity is parallel to a major crystal orientation, the ions pass through the crystal without any large-angle Rutherford scattering events. Hence the number of backscattered ions in RBS/C is drastically lower than for a measurement in a random direction (i.e a non-channeling orientation). RBS/C provides information on the lattice site location of impurities or lattice disorder. A lower number of backscattered ions in RBS/C, signifies higher crystallinity in the probed crystal orientation.

3.5 Secondary Ion Mass Spectrometry

This section is based on the text book by Leng [42]. *Secondary Ion Mass Spectrometry* (SIMS) is a technique widely used to determine which elements are present in a crystal. The technique is based on bombarding a sample with primary ions (usually Ar^+, Ga^+, Cs^+ or O^+), resulting in collisions and sputtering of secondary ions, neutral atoms and molecules from the sample. Only secondary ions is analyzed in a SIMS measurement, and the portion of sputtered particles which are ions is small ($\sim 1\%$). SIMS analysis can be divided into two modes; *dynamic*- and *static* SIMS. Dynamic SIMS measurements have a high flux of primary ions, which can remove

many atomic layers, and an elemental distribution as a function of depth in the crystal can be obtained. In static SIMS measurement a low flux of primary ions are incident on the sample, and only the surface is analyzed.

In order for the secondary ion not to be disturbed or to interact with other particles, ultra-high vacuum is required. The primary ions are generated by an *ion source* before entering an *ion filter*, where unwanted ions are filtered from the ion beam using electric- and magnetic fields. The beam is focused by electro-magnetic lenses and scanned over the sample surface by deflecting the ion beam using a *deflector*.

A *magnetic sector analyzer* is used for mass analysis of the secondary ions. The ions are accelerated by a potential before being influenced by a magnetic field perpendicular to their velocity. The electrically charged ions get a bent path as a result of this magnetic field, where the radius of the path curvature is mass dependent. Thus, by adjusting the magnetic field, only ions with the desired mass passes through the slit while undesired ions are filtered out. For depth profiling, a constant sputtering rate is used. The secondary ion intensity of each element analyzed is then plotted as a function of depth or sputtering time.

3.6 Photoluminescence Spectroscopy

This section is based on the review of Gilliand [48]. Photoluminescence (PL) spectroscopy is an important characterizing technique for analyzing the optical properties of semiconductors. By measuring and analyzing the energy distribution of emitted photons after optical excitation, properties such as the composition of the material, impurities and optical emission efficiencies can be obtained. Excitation is achieved by laser and after the photoluminescence is spectrally dispersed by a spectrometer it is detected by a photomultiplier tube.

Excited charge carriers can decay to lower energy states through different mechanisms. Band-to-band recombination, requires the presence of both an electron and a hole. An electron in the bottom of the conduction band recombining with a hole in the top of the valence band emits a photon with energy equal to the band gap. However, in certain materials this mechanism is relatively unlikely since an exciton is more stable, recombining through free-exciton recombination. An exciton is a quasi particle which can be generated through photon absorption, consisting of an electron and a hole separated by the bandgap but attracted to each other by the Coulomb interaction energy. The exciton can travel through the periodic structure and can hence transport energy without being electrically charged [49]. The main peak in a PL spectrum of a perfect material will be due to free-exciton recombination. Impurities may also serve as recombination centers, with different positions in the band gap depending on its chemical identity and charge state. A donor level lies in close proximity to the conduction band, and a conduction electron can decay to this level before recombining with a hole, and the opposite is true for acceptor levels. There are also so-called deep levels which lie somewhere in the middle of the band gap, and can act as recombination centers for charge carriers. Thus by analyzing a PL spectrum, different impurities in a thin film can be characterized.

3.7 Stylus Profilometry

This section is based on the work of Krüger-Sehm in the textbook "Encyclopedia of Tribology" [50]. Stylus profilometry is a topography technique somewhat similar to AFM. By etching away an area of a thin film leaving an abrupt edge between the film and substrate, a stylus

profilometer can measure the height difference and hence the thickness of the film. A sharp tip commonly made of diamond with a radius between 0.1 and 50 μm, is in contact with the surface, and is scanned horizontally. Any difference in the vertical direction during the scan, results in a height displacement of the tip and the measuring sensor converts this height difference into an electrical signal. During the scan, both the tip position and height is sampled in time or space intervals, and the profilometer gives an accurate analysis of the thin film thickness.

3.8 Hall effect measurements

This section is based on the textbooks by Streetman et. al. [6] and Kittel [9]. Hall effect measurements is a method for characterizing the resistivity, the charge carrier concentration and their Hall mobilities in a material. The method is based on the Hall effect, which describes how a voltage difference builds up in a material when a current is flowing and a magnetic field is present. If a magnetic field is present perpendicular to the velocity vector of a charge carrier, the carrier will experience the Lorentz force;

$$\mathbf{F} = -e(\mathbf{E} + \mathbf{v} \times \mathbf{B}) \tag{3.17}$$

Where $\mathbf{F}$ is the Lorentz force, e is the elementary charge, $\mathbf{E}$ is the electric field, $\mathbf{v}$ is the velocity vector of the charge carrier and $\mathbf{B}$ is the magnetic field. The Lorentz force will bend the path of the charges introduced into the material, as shown in figure 3.7. If the material is n-type and the current is not allowed to escape in the y-direction, electrons will accumulate at the left side as shown in figure 3.7. This accumulation will build up an electric field in the

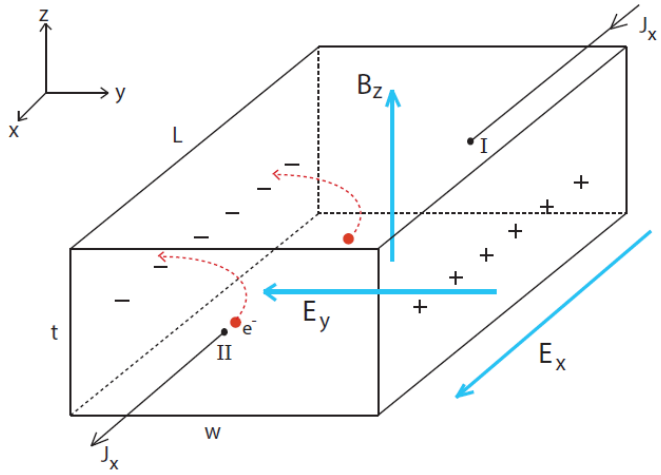

Figure 3.7: *The Hall effect on a sample with length L, width w and height t. A magnetic field B_z is perpendicular to the velocity of the electron v_x, which bends the path of the charge due to the Lorentz force. An electric field E_y is established perpendicular to both the magnetic field and the current density. Figure adapded from Kittel [9].*

y-direction, termed the Hall field, E_y. The build up of this field is known as the Hall effect. The field balances the product $v_x B_z$ (v_x is the electron velocity and B_z is the magnetic field)

to maintain a steady flow of electrons in the opposite direction of the current density. This means that equation (3.17) can be written

$$E_y = v_x B_z \tag{3.18}$$

Using equation (3.18) the electron velocity v_x is then

$$v_x = -\frac{J_x}{en} \tag{3.19}$$

where J_x is the current density, e is the elementary charge and n is the electron density. E_y can be expressed by

$$E_y = -\frac{J_x}{en} B_z = R_H J_x B_z \tag{3.20}$$

where R_H is called the Hall coefficient and is defined by

$$R_H \equiv -\frac{1}{en} \tag{3.21}$$

This means that if the current and the magnetic field are known, the electron concentration in the material can be calculated by measuring the electrical field which is built up perpendicular to both the current and the magnetic field. This relation can also be used to determine whether the material is n-type or p-type. Equations (3.17), (3.19), (3.20) and (3.21) need very few modifications if the material is p-type. Since the majority carriers in a p-type material are holes, p is used instead of n, and the sign in the equations is changed. The resistivity can be determined by a resistance measurement. If the voltage between point I and point II ($V_{I,II}$) in figure 3.7 is measured, the resistance and resistivity is given by:

$$R = V_{I,II}/I_x \rightarrow \rho = \frac{Rwt}{L} = \frac{V_{I,II}/I_x}{L/wt} \tag{3.22}$$

Where I_x is the current going through the sample with dimensions L,w,t. The resistivity is given by:

$$\rho = \frac{1}{\sigma} = \frac{1}{-en\mu_n} \tag{3.23}$$

The mobility in the sample can hence be expressed by the Hall coefficient:

$$\mu_n = \frac{\sigma}{-en} = \frac{R_H}{\rho} \tag{3.24}$$

If the majority carriers are holes, as in a p-type material, the mobility μ_p is found.

3.8.1 Van der Pauw Method

This subsection is based on the report by L. J. van der Pauw [51]. The Van der Pauw method is used to determine the resistivity, the mobility and the carrier concentration in a material. For determination of the specific resistivity and Hall effect of a flat sample of arbitrary shape, the Van der Pauw method demands the following conditions to be fulfilled:

- *The contacts are at the circumference of the sample.*
- *The sample is homogeneous in thickness.*
- *The contacts are sufficiently small.*
- *The surface of the sample is singly connected, i.e., the sample does not have isolated holes.*

Four contacts are placed in the corners of a sample, current is passed through two of them while the voltage is measured between the other two. The contacts in each corner of the sample are labeled 1-4 clockwise/counter-clockwise, and if the current enters the sample through 1 and leaves through 2, the potential difference between 3 and 4 (V_4-V_3) is measured. This current and potential difference defines the resistance $R_{12,34}$, with the following relations holding true:

$$\begin{aligned} I_{12} - V_{34} &\Longrightarrow R_{12,34} \\ I_{21} - V_{34} &\Longrightarrow R_{21,34} \\ I_{23} - V_{41} &\Longrightarrow R_{23,41} \\ I_{32} - V_{41} &\Longrightarrow R_{32,41} \\ I_{34} - V_{12} &\Longrightarrow R_{34,12} \\ I_{43} - V_{12} &\Longrightarrow R_{43,12} \\ I_{41} - V_{23} &\Longrightarrow R_{14,23} \\ I_{14} - V_{23} &\Longrightarrow R_{41,23} \end{aligned}$$

Using these resistances, two characteristic resistances R_a and R_b can be defined as:

$$R_a = \frac{1}{4}[R_{12,34} + R_{21,34} + R_{34,12} + R_{43,12}] \tag{3.25}$$

$$R_b = \frac{1}{4}[R_{32,41} + R_{23,41} + R_{14,23} + R_{41,23}] \tag{3.26}$$

and utilizing the Van der Pauw equation (3.27), the sheet resistance, R_{Sheet}, can be obtained:

$$e^{-\pi R_a/R_{Sheet}} + e^{-\pi R_b/R_{Sheet}} = 1 \tag{3.27}$$

$$R_{Sheet} = \frac{\pi}{ln2}\frac{R_a + R_b}{2} f(\frac{R_a}{R_b}) \tag{3.28}$$

Multiplying this R_{Sheet} with the thickness of the thin film, d, the resistivity is obtained.

$$\rho = R_{Sheet} * d \tag{3.29}$$

and the final expression of the resistivity is:

$$\rho = \frac{\pi d}{ln2}\frac{R_a + R_b}{2} f(\frac{R_a}{R_b})$$

where the last product is a function of the ratio R_a/R_b, which is equal to unity for $R_a = R_b$ while it decreases as the ratio increases.

3.9 Four-point Probe

This section is based on the articles by Smits [52] and Valdes [53]. An efficient way to calculate the resistivity of a thin film is by using Four-point probe. The technique uses four probes on a row with equal spacing. One of the outer probes sends out current which leaves the sample through the other outer probe. Hence, a potential difference arises between the outer probes, and this potential difference is measured by the two inner probes. The sheet resistivity, ρ_s, for an semi-infinite sample, with the probe spacing s, is given by

$$\rho_s = 2\pi s \frac{V}{I} \tag{3.30}$$

Where I is the current sent from one outer probe to the other, and V is the potential difference measured by the inner probes. For a thin film of finite thickness, ω, where the thickness of the conducting film is less than 40% of the probe spacing s, the resistivity is given by;

$$\rho = \rho_s \omega = \omega \frac{V}{I} \frac{\pi}{ln2} F(\omega/s) \tag{3.31}$$

where ω is given in cm. The function F(ω/s) is a correction factor which is equals 0.9214 for ω = s and goes to unity when ω/s approaches zero [52].

Chapter 4

Results

4.1 Experimental Equipment and Procedures

4.1.1 Equipment

4.1.1.1 Magnetron Sputter

The thin film deposition was done with a Semicore Tri-Axis balanced field magnetron sputtering system. Both DC and RF sputtering are available. Three targets can be used individually or simultaneously, which makes co-sputtering possible. Circular $3''$ targets are utilized, and the ZnO target used in this study was 99.99% pure ZnO. The target distance from the substrate holder was 10 cm with an angle of $\sim 18°$ to the substrate normal.

4.1.1.2 Stylus Profilometer

The profilometry was done using a Veeco Dektak 8. A 1:20 HCl:H_2O solution was used for etching of the areas not covered with photo resist.

4.1.1.3 XRD

X-ray diffraction measurements of the thin films were made by a Bruker AXS D8 Discover system. The x-ray source was Cu, which has characteristic emission peaks with wavelengths $k_{\alpha 1}$ = 1.5406 Å and $k_{\alpha 2}$ = 1.54444 Å. A Ge (220) double bounce monochromator was implemented to filter out the $k_{\alpha 2}$ signal.

4.1.1.4 RBS

RBS analysis of the thin films was realized using a 1 MV Tandem ion accelerator (National Electrostatics Corporation). The probing beam consisted of 3.045 MeV He^{++} ions for the 600°C samples and 1.62 MeV He^{+} ions for the 400°C samples, incident along the [0001] direction. The beam was backscattered with an 165° angle with respect to the incident beam into the detector.

4.1.1.5 PL

Photoluminescence was done employing a 325 nm wavelength continuous He-Cd laser with an output power of 10 mW as an excitation source. Emission was collected by a microscope and

directed to a fiber optic spectrometer (Ocean Optics USB4000, spectral resolution 2 nm).

4.1.1.6 AFM

The tapping mode Atomic Force Microscopy measurements were done using a Veeco Dimension 3100 Atomic Force Microscope. For tuning fork mode, a Multiview 2000 SPM system was employed. The AFM probe used in tuning fork is coated with Cr, has a resonant frequency of 32.71 kHz and a Q factor of 2000.

4.1.1.7 SIMS

SIMS measurements were done utilizing a Cameca IMS-7f microanalyzer that combines both scanning ion microprobing and ion microscope. It is also equipped a Duoplasmatron (O_2) and a cesium primary ion source, an electrostatic sector analyzer, a magnetic sector analyzer and three detectors. The three detectors are an electron multiplier, a Faraday cup and a fluorescent screen. The ions used in the measurements were 10 keV O_2^+.

4.1.1.8 Hall Effect Measurements

For Hall effect measurements a Keithley 6221 current source, a Keithley 2182 nanovoltmeter and a Keithley 7001 (w 7065) switch system were used. The samples were measured in the van der Pauw geometry.

4.1.1.9 Four-point Probe

Resistivity measurements was done with a Jandel KM3-AR. The current range for direct current is 10nA-99mA. A probe designated for ZnO measurements was used.

4.1.2 Sample Preparation

A 2x2 cm^2, highly resitive ZnO substrate purchased from Tokyo Denpa was cut using a diamond pen into several smaller samples with an approximate dimension of 5x5 mm^2. The substrate was grown using the hydrothermal method [54] and the dimensions, miscut and resistivity can be seen in table (4.1). Figure 4.1 shows the top view of the substrate, with the m- and a-axis in the surface plane and c-axis perpendicular to the surface. Before deposition the substrates were cleaned. The cleaning procedure was 10 minutes in acetone before directly placed in isopropanol for 10 minutes followed by 10 minutes in de-ionized water. In all these three steps, the holder was placed in an ultrasonic bath and the substrates were placed in the holder with the Zn-face up to avoid potential scratches on the substrate surface. Before inserted in the sputter chamber the substrates were dried in nitrogen flow. The deposition was done on the substrate Zn-face.

Before the temperature dependency depositions were started, a cleaning series was done to find which duration of the acetone cleaning step gave the surface the lowest roughness and thus most suited for homoepitaxial growth. Five substrates were cleaned with different acetone treatment durations; 10 minutes, 5 minutes, 3 minutes, 2 minutes and 1 minute. The 2 minutes duration was found to give the best surface preparation, and this cleaning procedure was then used for one of the high temperature depositions, while the other substrate was cleaned the same way as the power series.

A	20 mm
B	20 mm
Thickness	515 μm
Off-Angle m-axis	0,00°
Off-Angle a-axis	0,03°
Resistivity	1419,00 Ωcm

Table 4.1: *Substrate dimensions and properties.*

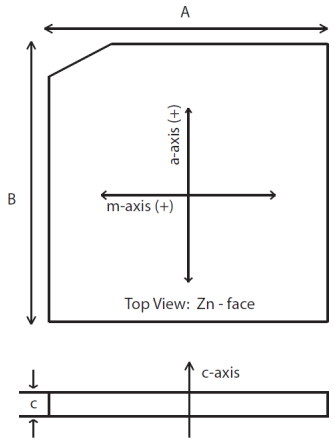

Figure 4.1: *Top view of highly resistive ZnO substrate grown in the (0001).*

4.1.3 Treatment of Errors

4.1.3.1 Stylus Profilometer

Five measurements were done for each sample. The average was taken from these five measurements and the standard deviation was calculated.

4.1.3.2 XRD

Because of the duration of the x-ray characterization procedure, only one measurement was done per sample. A Gaussian fitting using the Origin 8.6 (Academic) software was used for calculating the peak position and full width at half maximum. A fitting will not be 100% equal to the original curve, and thus standard error of the calculated peak position and FWHM is given. The listed values of the FWHM takes into account the instrumental broadening. Since a Gaussian fitting has been utilized, the actual FWHM has been calculated to be:

$$\beta = \sqrt{\beta_{mea}^2 - \beta_{ins}^2} \tag{4.1}$$

where β_{mea} is the measured FWHM and β_{ins} is the contribution from instrumental broadening.

4.1.3.3 AFM

Three measurements were done per sample with the AFM. The roughness was calculated using the WSxM 5.0 Develop 7.0 software. The average and standard deviation were calculated from the three measurements per sample.

4.1.3.4 Hall Effect Measurements

The samples were measured in the van der Pauw geometry. Three resistivity measurements were done, and four measurements for the carrier concentration and Hall mobility were done. In addition three resistivity measurements were done with the Four-point probe. The average of these quantities as well as the standard deviation were calculated.

4.2 Power series

A power series was made in the spring of 2014 with a sputter chamber pressure of 21 mTorr, and the results of this study can be seen in appendix A. Due to the low crystal quality of this series, the chamber pressure was reduced. In addition, the magnetron sputter at MiNaLab was during 2014 optimized in terms of the target angle with respect to the substrate holder, see appendix B. This optimization was made to increase the uniformity of the deposited thin films. These optimizations gives the possibility of thin films with excellent crystal quality and epitaxial growth. The power series was deposited on highly resistive ZnO c-axis oriented bulk substrates using sputter deposition. Eight different thin films were deposited, where the deposition power was varied. 10W, 20W, 30W, 40W, 50W, 70W, 90W and 110W was used, and the depositions were not started until the pressure reached 2×10^{-6} Torr. The deposition durations were: 91 minutes (110W), 111 minutes (90W), 143 minutes (70W), 200 minutes (50W), 250 minutes (40W), 333 minutes (30W), 500 minutes (20W) and 1000 minutes (10W). All substrates were annealed at 400°C for 30 minutes in the sputter chamber prior to deposition. Presputtering was done for 15 minutes to remove impurities in the target material. During deposition, the chamber pressure was 7.1 mTorr and the inert gas used was Ar at a flow rate of 50 sccm. The substrate was kept at 400°C during deposition. Rotation of the substrate during deposition was set to 11 rpm. In addition to the ZnO substrate, silicon substrates were also placed in the chamber during all depositions. The ZnO thin films on the Si substrates were partially etched away to measure their thickness using Stylus Profilometry. The crystal-, electrical- and optical properties as well as surface morphologies were characterized using XRD, PL, RBS, AFM and Hall effect measurements to investigate the influence of the deposition power on the quality of the thin films and hence get one step closer to achieving homoepitaxial growth using sputter deposition.

4.2.1 Thickness measurements

To determine the deposited thin film thickness, ZnO was also deposited on Si substrates. All Si substrates were cleaned using RCA cleaning, while immediately before deposition the Si substrates were cleaned the same way as the ZnO substrates. After deposition the ZnO deposited on Si was baked at 120°C for 10 minutes to remove moisture on the surface, before a small part of the ZnO film was covered by photo resist. The samples were then baked a second time at 120°C for 20 minutes to ensure good adhesion between the photo resist and the thin film. In a 1:20 HCl:H_2O solution, the exposed thin film was etched off. The etching duration was a couple of seconds, where the full removal of the oxide could be seen as a rapid color change. The samples were then rinsed in water for several minutes. Using Stylus profilometry, the height difference between the film and the substrate was measured at five different positions on each sample. In figure 4.2 the measured thicknesses are shown. The goal was to obtain films with a thickness around 500 nm, where the two samples deposited first gave deposition rates used to estimate the deposition duration for the remaining samples. As can be seen in the section 4.2.4, the growth rate for ZnO on ZnO is not the same as for ZnO on Si.

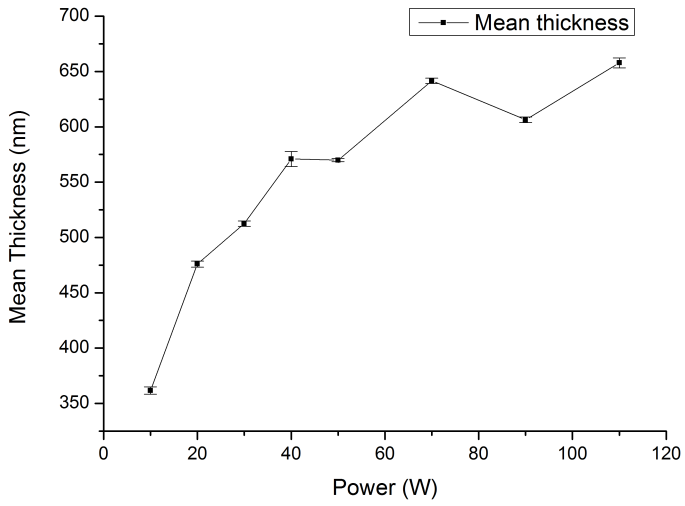

Figure 4.2: *Thickness measured using Stylus profilometry of the ZnO deposited on Si films.*

4.2.2 X-Ray Diffraction

For investigating the interplanar spacing d, as well as strain and stress in the deposited films, $\theta/2\theta$ scan was utilized. The substrate used for reference is from a different wafer, but the same batch as the substrates used for the thin film depositions. As seen in figure 4.3 the intensity is plotted as a function of 2θ for all samples in the power series around the (0002) peak of ZnO.

The figure shows that the low power samples posses a narrower peak than the high power samples, i.e. the 10W and 30W samples have very narrow peaks with a Gaussian shape. Further, the 10W and 30W peak positions coincide with the substrate peak position. This means that the films have an interplanar spacing in the direction perpendicular to the surface equal to that of the substrate. For the 10W and 30W samples, a small elevation is seen on the right side of each peak. By examining the substrate reference, the same elevation is observed and is thus caused by the substrate. For some of the samples such as the ones deposited with 40W and 50W, a small elevation can be observed on the left side of the peak indicating that a small fraction of the grains have a different interplanar spacing with respect to the rest. The high power samples, especially 70W, 90W and 110W, posses broader main peaks evidencing a higher defect density in these samples which can be explained by the high deposition power. For higher effects during deposition, the sputtered atoms posses more energy than for low powers, causing damage to the substrate and reducing the crystal quality for higher deposition powers. For the 90W and 110W samples, distinct side-peaks is also observed. The side-peak is clear evidence that the film and substrate posses different interplanar spacings d. The samples deposited at 20W and 40W also appear to have lower quality. For the 40W sample, this deviation from the power series crystal quality trend, can be explained by instrumental failure during deposition. The film deposited at 20W power also differs from this trend. The crystal quality of this sample should be close to the 10W sample, but a significant broadening of the peak is observed. The cause of this is uncertain, but it is suspected that something went wrong during deposition.

From the $\theta/2\theta$ scan, the strain and stress in the films were also calculated and can be seen

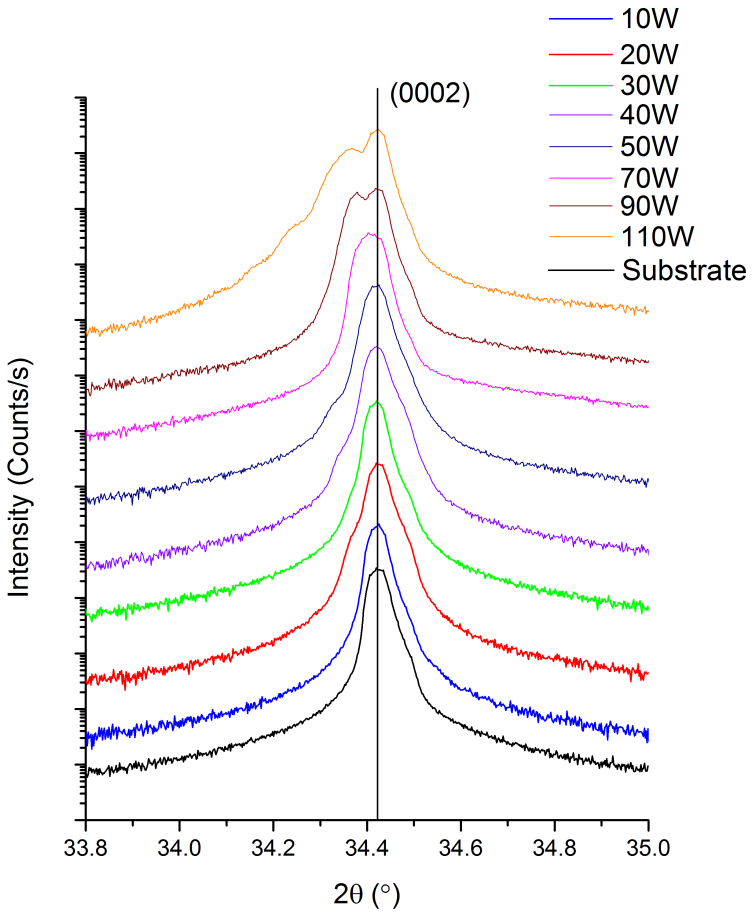

Figure 4.3: *The θ/2θ scan of all the samples in the power series around the (0002) peak for ZnO. For the 10W sample the peak is relatively narrow, while a broadening is observed as the power is increased. The 90W and 110W samples differ from the other samples by the emergence of a side peak.*

in figure 4.4. The figure also displays the highest crystal quality for the films deposited with low power. Both strain and stress increase drastically for the samples with powers higher than 50W, and is explained by the damage to the substrate during deposition. The damage to the substrate surface causes the film to grow non-epitaxially, which again causes stress and strain in the film. The extracted $\theta/2\theta$ scan parameters and the calculated strains and stresses is seen in table (4.2). Using Rocking Curve scans, lattice planes parallel to the surface were

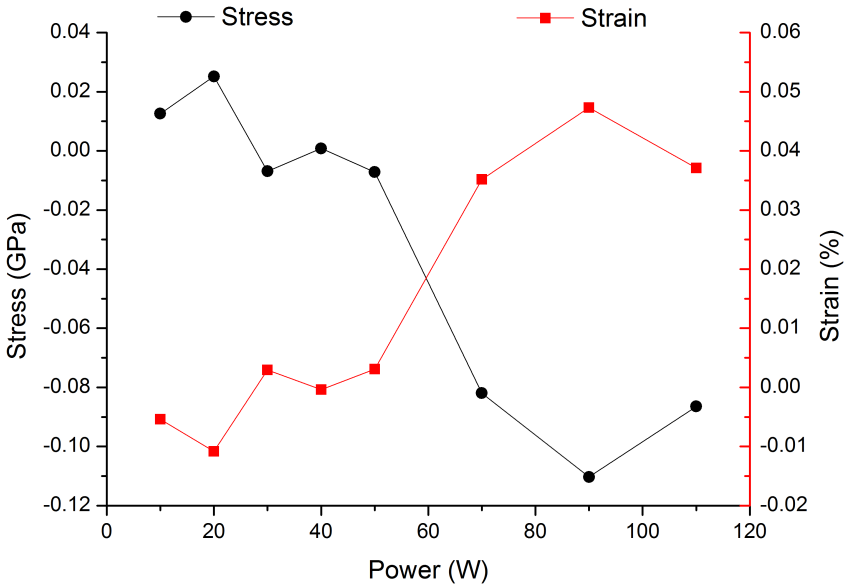

Figure 4.4: *Strain perpendicular to the surface (red) and stress parallel to the surface (black) calculated for all samples in the power series. The samples deposited at low powers exhibit low strains and stresses. A drastic increase in both strain and stress is seen for the samples deposited at 70W and higher.*

evaluated by investigating the (0002) peak of the $\theta/2\theta$ scans. For the samples with two peaks (90W and 110W) the peak corresponding to the thin film was investigated. From figure 4.5, it is clear that the low deposition power, with the exception of 20W and 40W, yields the highest crystal quality.

A narrow peak in the rocking curve scan signifies low, or no, tilt in the lattice planes (nearly) parallel to the surface. The 10W and 30W samples shows the best results from the rocking curve scan, with narrow peaks, which can be seen from the FWHM values of 0,010° and 0.015° respectively. In comparison Kim et.al. [31] reported homoepitaxial growth of ZnO with rocking curve FWHM values of 0,003° - 0,018°. The films deposited at 50W or higher have broader rocking curve peaks, meaning that the grains posses a distribution of tilts, possibly originating from edge- and screw dislocations. A broader peak can thus be interpreted as a higher concentration of edge- and screw dislocations in the film compared to samples with a lower FWHM value. The 110W sample has the broadest peak, indicating the poorest crystal quality, corroborating the hypothesis of better crystal quality for lower deposition powers. It is also clear, like for the $\theta/2\theta$ scan, that the 20W and 40W samples are somewhat degraded. In table (4.3) it can be seen that the FWHM increases for increasing deposition power, underlining the qualitative analysis of the peak shapes, stating a higher

Table 4.2: Extracted $\theta/2\theta$ scan parameters for the power series:

Sample	2θ peak (^{0})	Std. Error (^{0})	FWHM (^{0})	Std. Error. (^{0})	Strain	Stress (GPa)
10W	34,422	$8{,}052*10^{-3}$	0,039	$1{,}233*10^{-4}$	$-5{,}403*10^{-5}$	$1{,}259*10^{-2}$
20W	34,424	$8{,}063*10^{-3}$	0,042	$1{,}498*10^{-4}$	$-1{,}081*10^{-4}$	$2{,}519*10^{-2}$
30W	34,419	$8{,}048*10^{-3}$	0,039	$1{,}129*10^{-4}$	$2{,}964*10^{-5}$	$-6{,}907*10^{-3}$
40W	34,420	$8{,}068*10^{-3}$	0,045	$1{,}626*10^{-4}$	$-3{,}601*10^{-6}$	$8{,}390*10^{-4}$
50W	34,419	$8{,}049*10^{-3}$	0,045	$1{,}163*10^{-4}$	$3{,}077*10^{-5}$	$-7{,}170*10^{-3}$
70W	34,408	$8{,}085*10^{-3}$	0,057	$2{,}032*10^{-4}$	$3{,}518*10^{-4}$	$-8{,}197*10^{-2}$
90W	34,403	$8{,}396*10^{-3}$	0,081	$9{,}536*10^{-4}$	$4{,}733*10^{-4}$	$-1{,}103*10^{-1}$
110W	34,407	$8{,}101*10^{-3}$	0,091	$1{,}470*10^{-3}$	$3{,}710*10^{-4}$	$-8{,}644*10^{-2}$
Substrate	34,424	$8{,}066*10^{-3}$	0,041	$1{,}556*10^{-4}$		

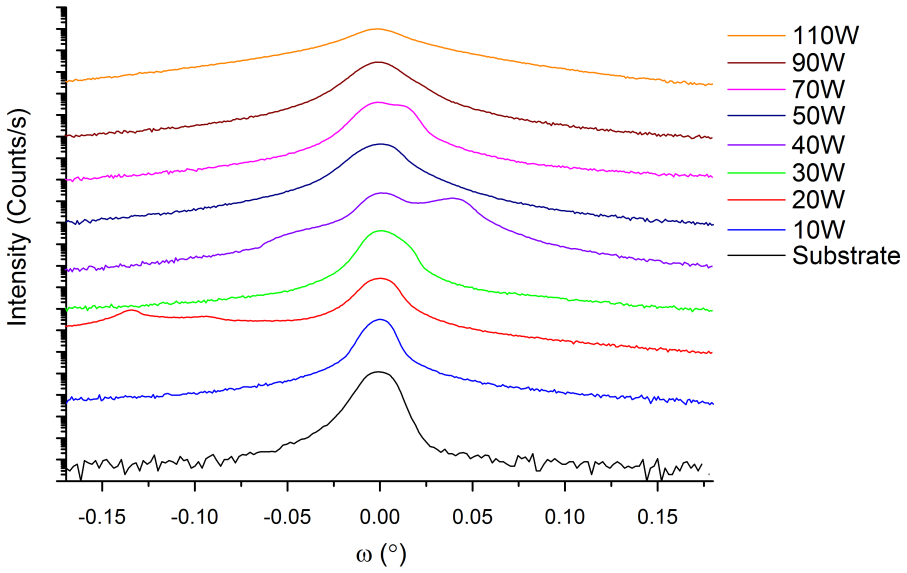

Figure 4.5: *Rocking curve scans of the (0002) peak of ZnO for all samples in the power series. A Rocking curve scan of the substrate is included as reference. The low power samples have the narrowest peaks, except 20W and 40W, which are degraded.*

Table 4.3: Extracted Rocking Curve scan parameters for the power series:

Sample	θ peak (^{0})	Std. Error (^{0})	FWHM (^{0})	Std. Error. (^{0})
10W	17,188	$8{,}019*10^{-3}$	0,010	$4{,}566*10^{-5}$
20W	17,231	$8{,}030*10^{-3}$	0,014	$7{,}069*10^{-5}$
30W	17,224	$8{,}028*10^{-3}$	0,015	$6{,}690*10^{-5}$
40W	17,227	$8{,}659*10^{-3}$	0,054	$1{,}630*10^{-3}$
50W	17,297	$8{,}035*10^{-3}$	0,020	$8{,}327*10^{-5}$
70W	17,245	$8{,}074*10^{-3}$	0,023	$1{,}786*10^{-4}$
90W	17,216	$8{,}039*10^{-3}$	0,019	$9{,}236*10^{-5}$
110W	17,179	$8{,}080*10^{-3}$	0,033	$1{,}905*10^{-4}$
Substrate	17.220	$8{,}029*10^{-3}$	0,012	$6{,}866*10^{-5}$

crystal quality for low deposition power.

ϕ scans were used to investigate possible rotational twists about the c-axis. The peaks position as a function of the angle, does not yield much information, as this depends on sample placement on the stage. The information in the ϕ scan lies in the number of peaks and any potential side-peaks. The ϕ scan results of the $(10\bar{1}5)$ peak of ZnO are shown in figure 4.6a exhibits six peaks, demonstrating the six-fold symmetry of ZnO. In figure 4.6a side-peaks is observed for most of the sample. Side-peaks can be interpreted as the $(10\bar{1}5)$ plane of the films is rotated with respect to the $(10\bar{1}5)$ plane of the substrate. The ϕ scan of the $(11\bar{2}4)$ peak of ZnO, shown in figure 4.6b, also has six peaks. No side-peaks are observed in figure 4.6b, meaning no in-plane rotation of the $(11\bar{2}4)$ plane of the films with respect to the substrate.

4.2.3 Rutherford Backscattering Spectrometry

The crystal quality of the power series samples were also examined by Rutherford Backscattering Spectrometry (RBS). The RBS measurements were done by Dr. Alexander Azarov. Figure 4.7 presents the results of both the random- and channeling mode of RBS. The almost indistinguishable lines at the top of the figure corresponds to the random mode, i.e. where ions are incident on the sample surface without any specific direction. When ions are incident in a random direction, a much larger number of backscattering events will occur. The other lines corresponds to the channeling measurement (RBS/C) results. At approximately channel number 400, the thin film surfaces are hit by the ions and the number of backscattered ions increase from zero. The low power samples, i.e. 10W, 20W and 30W have a lower number of backscattering events than the remaining samples. This is due to the lower mean free path (distance between scattering events) of the ions, which again means that the crystal quality is higher and the defect- and dislocation concentrations are lower. The two samples deposited at 90W and 110W have the largest number of backscattering events, and hence the lowest crystal quality. The surface minimum yield (i.e. RBS/C / RBS-random at the surface) for the 90W sample is $\sim 6\%$, which is the highest for the power series, while for the low power samples (10W-30W) the surface minimum yield is $\sim 2\%$. The surface minimum yields of the low power samples matches that of single crystal ZnO grown by the hydrothermal method [55], indicating the thin films crystal perfection matches that of the substrate.

Another interesting observation that can be made is the shape of the RBS/C results. For the 90W and 110W samples, the yield increases in a $\sqrt{x}$ fashion for decreasing channel numbers

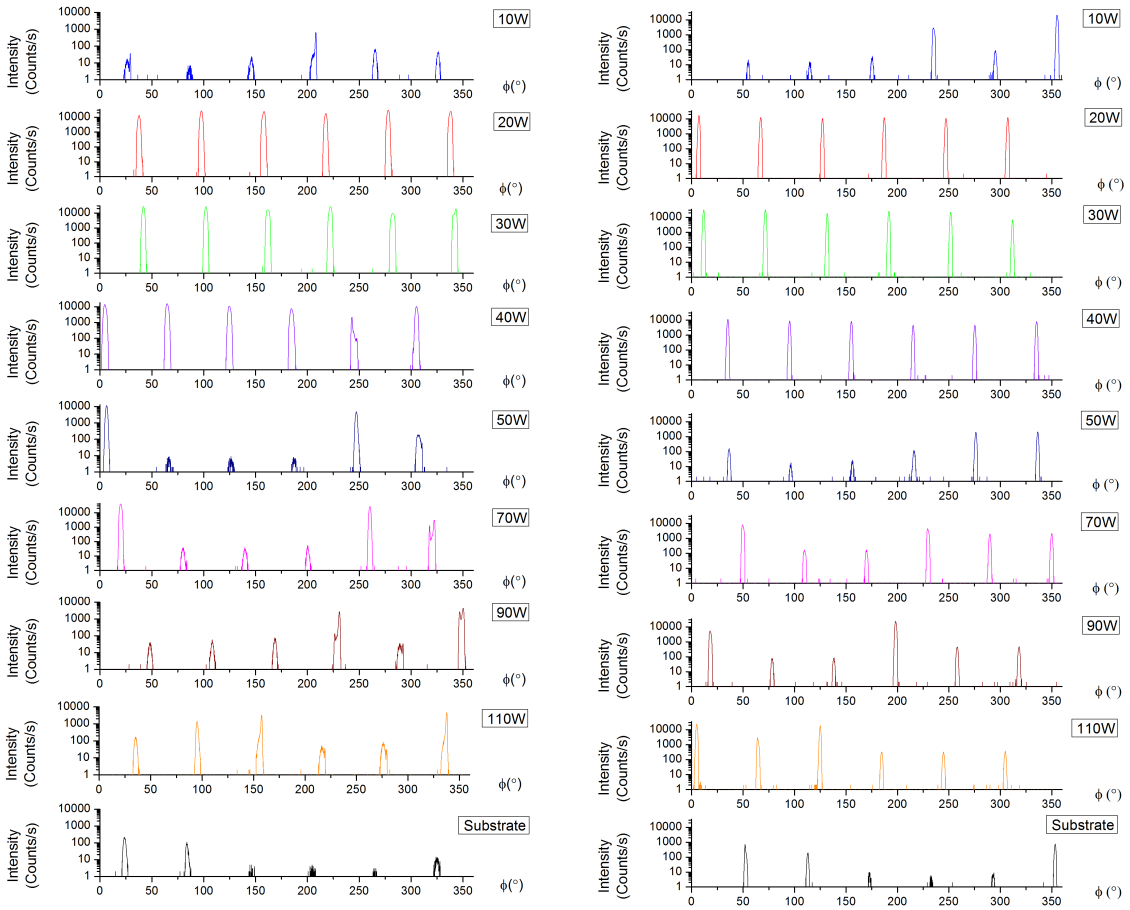

(a) (b)

Figure 4.6: ϕ scan of the $(10\bar{1}5)$ (a) and the $(11\bar{2}4)$ (b) peak of ZnO for all samples in the power series. All samples show six peaks, corresponding to the six-fold symmetry of ZnO.

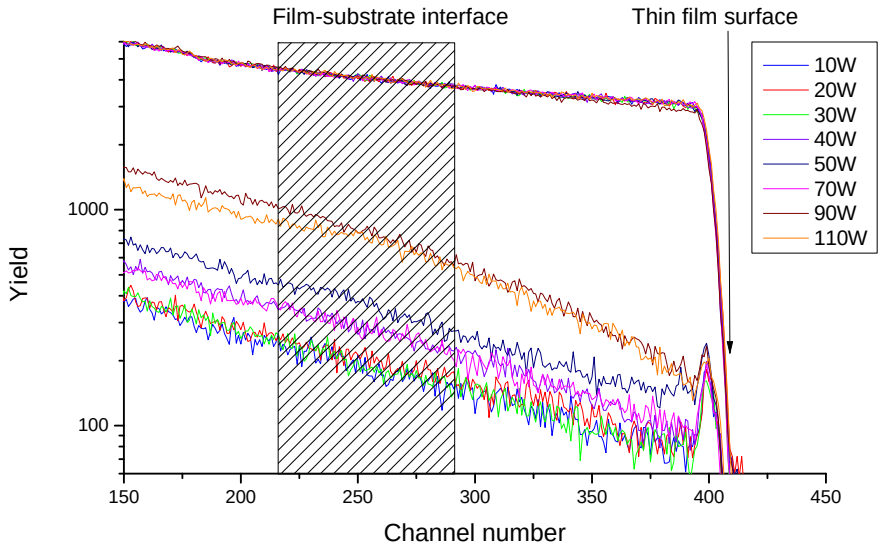

Figure 4.7: *Rutherford Backscattering Spectrometry results for the power series. The almost indistinguishable lines at the top of the figure corresponds to RBS done in random mode. The remaining lines represents the RBS/C results. The marked area shows at which channel number the film-substrate interface can be expected to be found for each sample.*

until at a certain channel number the yield-channel number dependencies seems to become linear. At this channel number the thin film-substrate interface can be found. With the two different slopes, it is possible to distinguish between substrate and film which points towards a non-epitaxial growth. For lower deposition powers it is harder to distinguish between the substrate and the film. For the 10W, 20W and 30W samples, the slope appears relatively linear throughout the whole sample, meaning that the film's crystal channels matches the ones of the substrate.

4.2.4 Secondary Ion Mass Spectrometry

SIMS measurements were done to characterize the Li, Na and Al concentrations in the power series samples. The SIMS measurements were done by Thomas Neset Sky. In figure 4.8 the concentration of Li atoms as a function of depth is shown for the samples. The concentration can be seen to increase rapidly at a certain depth before stabilizing. For some samples a peak appears before the concentration stabilizes. The depth of this peak, or where the rapid increase in concentration ends, is where the thin film-substrate interface is located. For the 10W, 20W and 30W sample, a rapid decrease in Li concentration from the bulk ZnO to the thin film surface can be observed. For the remaining samples the decrease in Li atoms is not as abrupt. The 20W and 30W samples also posses less Li than the remaining samples, while the 70W, 90W and 110W samples have the highest concentrations. The Li concentration is at least 2 orders of magnitude larger in the bulk compared to the thin films and, the Li is not incorporated during deposition. The substrates therefore contains a relatively high concentration of Li and the Li atoms diffuse into the film during growth.

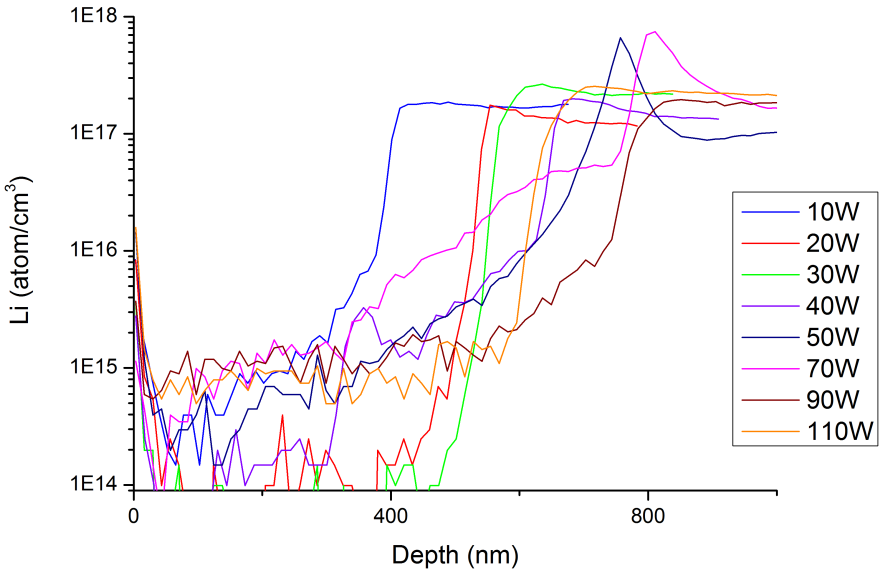

Figure 4.8: *SIMS measurement showing the Li concentration in the power series samples as a function of depth.*

In figure 4.9 the Na concentration as a function of depth can be seen. This plot can also easily be used to determine the thin film thicknesses, due to the distinct peaks that appear at the thin film-substrate interface. The Na concentration vs. depth have a U-shape, where the highest concentrations are found close to the surface and at the film-substrate interface. This can be understood as human sweat, since the film- and the substrate surfaces are the only areas exposed to human contact. The films deposited at 70W, 90W and 110W contain most Na atoms, while the 20W sample have the highest concentration at both the surface and interface between film and substrate.

Figure 4.10 shows the Al concentration in the power series samples. A relatively high concentration ($\sim 10^{18}$ cm^{-3}) can be seen for all samples, and is most likely incorporated during deposition by unwanted sputtering of the walls of the sputter chamber. Also for Al the U-shape of the concentration vs. depth plot can be observed, with maximums at the surface and film-substrate interface. The maximum at the film-substrate interface may be explained by the pre-deposition annealing, where Al atoms could be deposited without any ZnO growth. From the SIMS measurements yielding the Na concentration in the films, the peak position corresponding to the film-substrate interface for each sample is the thin film thickness. The thicknesses of the individual thin films can be seen in table 4.4.

4.2.5 Photoluminescence

Photoluminescence (PL) spectroscopy was utilized to characterize the optical properties of the power series samples. The PL measurements were done by Dr. Augustinas Galeckas. In figure 4.11 the near-band edge emissions are displayed. The figure also shows the suggested mechanisms causing the emissions (vertical lines), where the DX (donor-bound exciton) gives the most prominent peak, at about 3.36 eV. The low power samples, especially 10W and 20W,

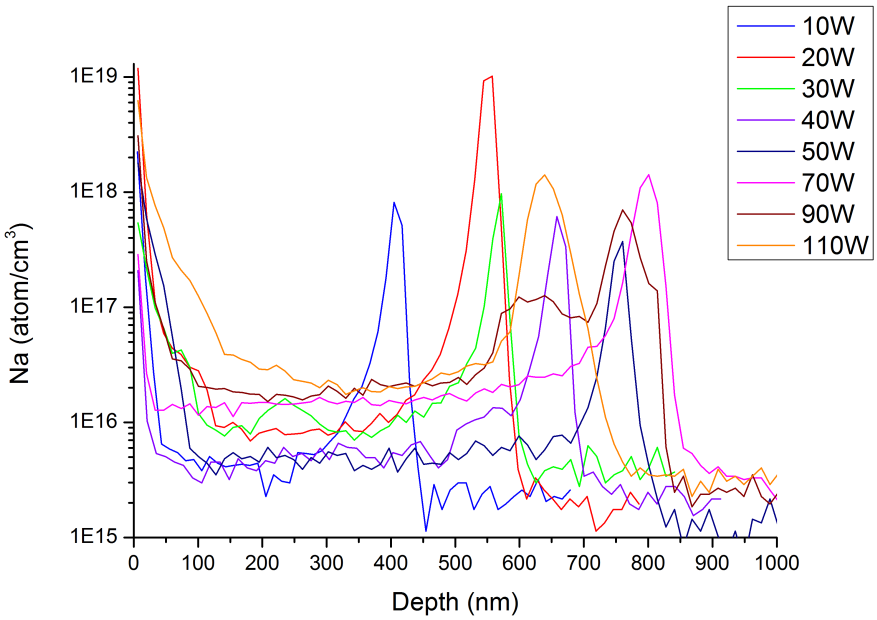

Figure 4.9: *SIMS measurement showing the Na concentration in the power series samples as a function of depth.*

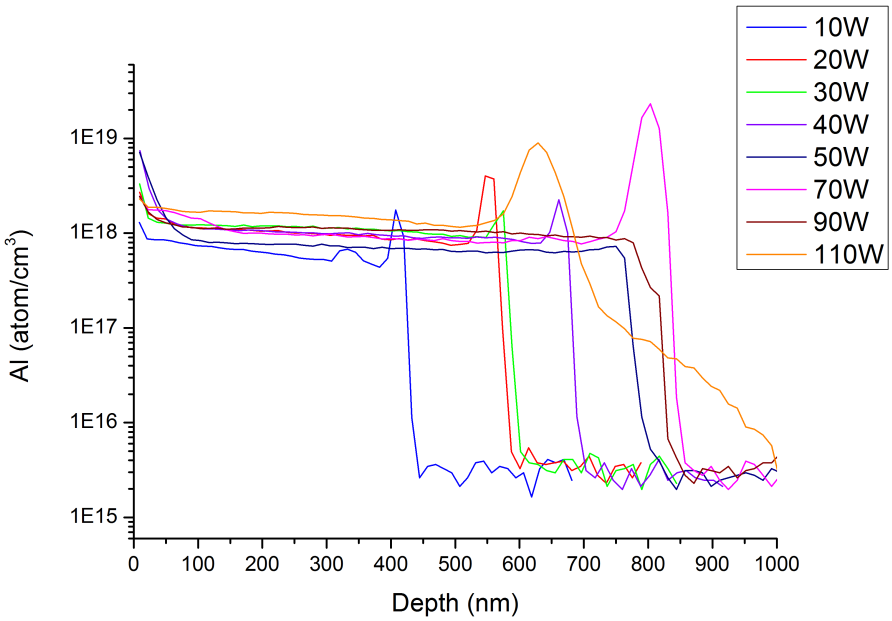

Figure 4.10: *SIMS measurement showing the Al concentration in the power series samples as a function of depth.*

Table 4.4: Thin film thickness obtained from SIMS results.

Deposition Power (W)	Thickness (nm)
10	405
20	557
30	572
40	658
50	760
70	801
90	760
110	638

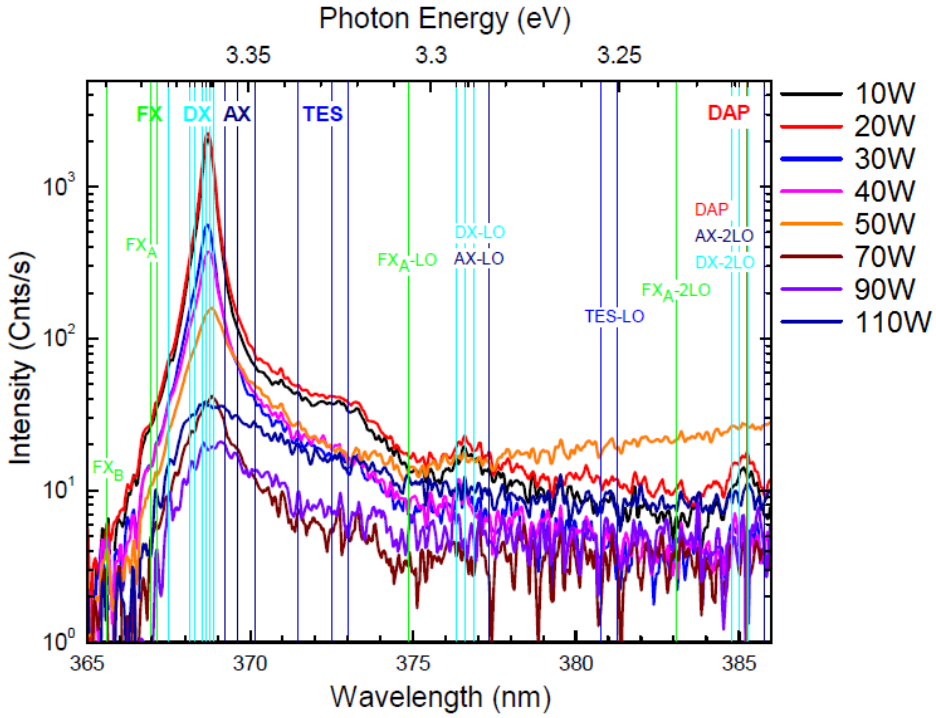

Figure 4.11: *Near-band edge PL emission of the power series samples.*

exhibits the highest intensity and lowest FWHM for this peak. This can be interpreted as less defects in the near-band edge region of the energy spectrum contributing to non-radiative recombination, and thus higher crystal quality. The samples deposited at 30W and 40W also exhibits distinct peaks, although with lower intensity. For the high power samples, the peak is quenched, signifying that more defects contribute to non-radiative recombination and these samples have a lower crystal quality. Small elevations on the left hand side of the donor-bound exciton peak can also be observed for the low power samples (10W-40W). The position in the energy spectrum where these elevations can be observed is the same position as the emission from free-excitons. Hence these elevations can be interpreted as corresponding to free-exciton emission. The PL plot including energies from deep level emissions is shown in figure 4.12.

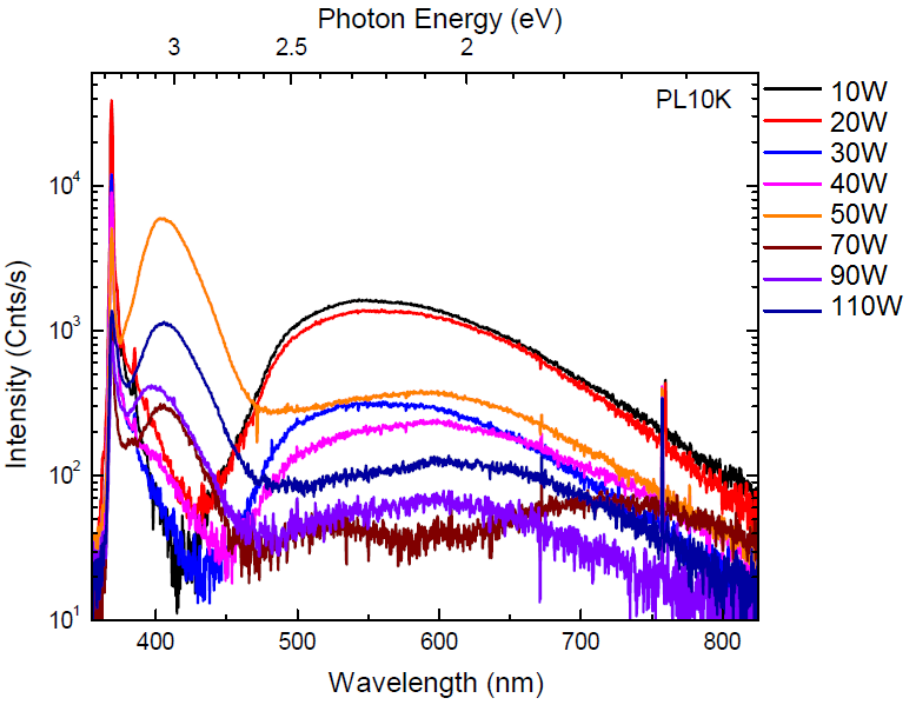

Figure 4.12: *PL measurement showing a broader spectrum incorporating shallow- and deep level defects.*

In the figure both shallow- and deep impurities can be observed. The widest peak (spreading from about 2-2.5 eV) can be attributed to deep level defects. For the low power samples the emission from this area exhibits a wide peak, like a band. For the high power samples on the other hand the peak shape changes, and thus yields that there are most likely more than one defect contributing to the emission. The low power samples exhibits higher intensities for these defects than the high power samples. A peak corresponding to emission from a defect with a shallower position in the band gap is observed at approximately 3 eV. For this peak, the trend is opposite to that of the deep level defects, as the low power samples exhibits lower intensities. The trend deviation is the 50W sample, which has the highest intensity of all the samples for the shallow defect. The specific shallow- and deep level defects these emission peaks arise from are subjects of discussion [15, 56, 57]. The defect at 3 eV may originate from interstitial zinc, which is a shallow donor [18], while the deep level defects can possibly be designated to defects such as interstitial oxygen, oxygen vacancies and zinc vacancies.

4.2.6 Atomic Force Microscopy

Atomic Force Microscopy (AFM) was utilized to characterize the surface topology of the thin films, using tapping mode. The morphology of the samples can, along with XRD, RBS and PL results give a clearer picture of the epitaxial growth of the thin films. The AFM measurements were made with a probed area of 2x2μm^2 and three measurements were made for each sample. In figure 4.13a - 4.13d the samples deposited at 10W to 40W, respectively, can be seen. The most important observation from these images is that the thin films are not completely flat single crystals. The thin films are instead composed of several small grains

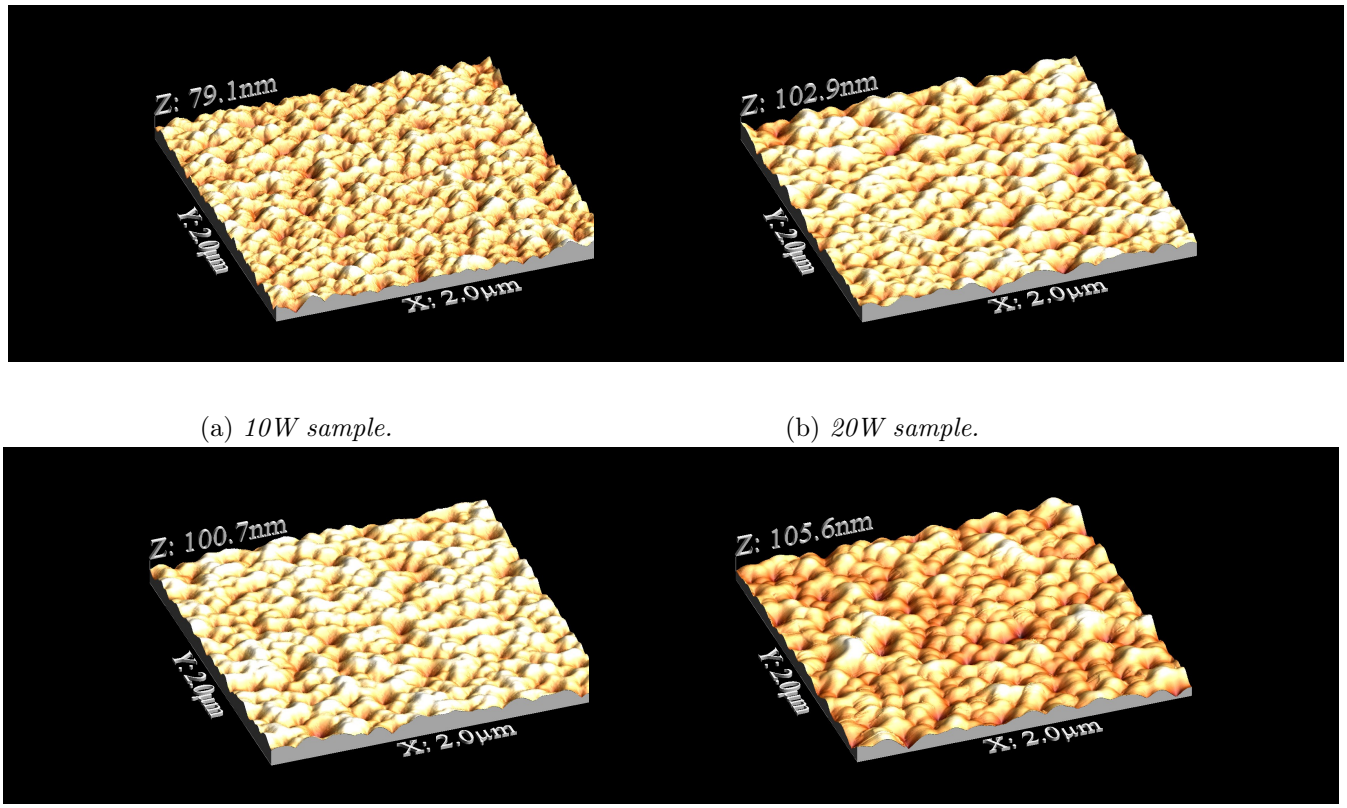

(a) *10W sample.* (b) *20W sample.*

(c) *30W sample.* (d) *40W sample.*

Figure 4.13: Three dimensional AFM images for samples deposited at 10W to 40W. A larger grain size is seen for increasing deposition effects.

which have grown vertically. Further, the lateral grain size increases for increasing deposition power. This observation is clearer when comparing the AFM measurements for the low power samples with those deposited at high powers 4.14a - 4.14d. The thin films deposited at high power, exhibits larger grains and a higher roughness. This is due to the higher deposition power results in higher surface mobility of the adatoms. The roughness of the thin films increase with increasing deposition power, as seen in table (4.5). The roughness of the low power samples does not show large variations, while the high power sample surfaces on the other hand contains either large peaks or pits leading to a higher roughness.

4.2.7 Hall Effect Measurements

The electrical properties (resistivity, carrier concentration and Hall mobility) of the thin films were measured with Hall effect measurements. The resistivity was also measured with four-point probe. In both techniques the thickness obtained from the SIMS measurements was used. In figure 4.15 the electrical properties of the power series are presented as a function of deposition power. The carrier concentration increases with increasing deposition power (especially evident for the 90W and 110W samples). The high carrier concentration might be explained by incorporation of hydrogen and Al during deposition, which as previously stated (2.4.2) always acts as donors in ZnO, or by a higher concentration of defects. From

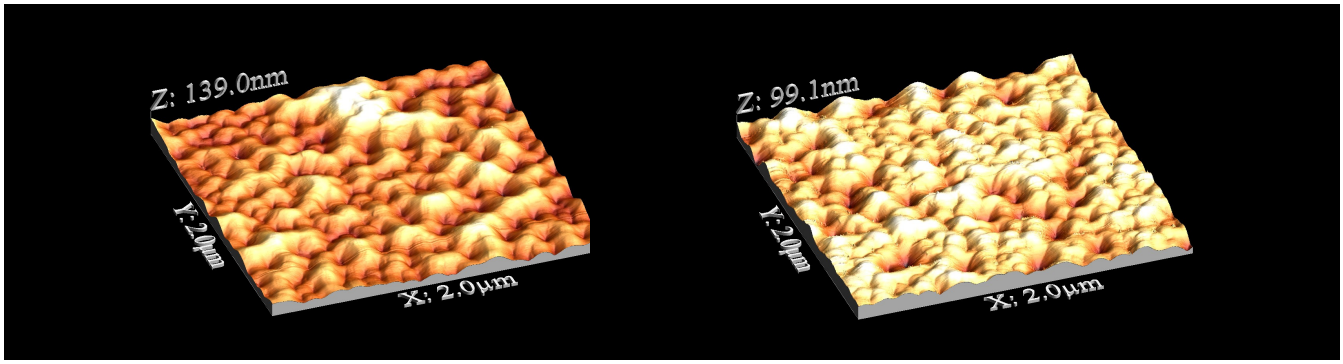

(a) *50W sample.* (b) *70W sample.*

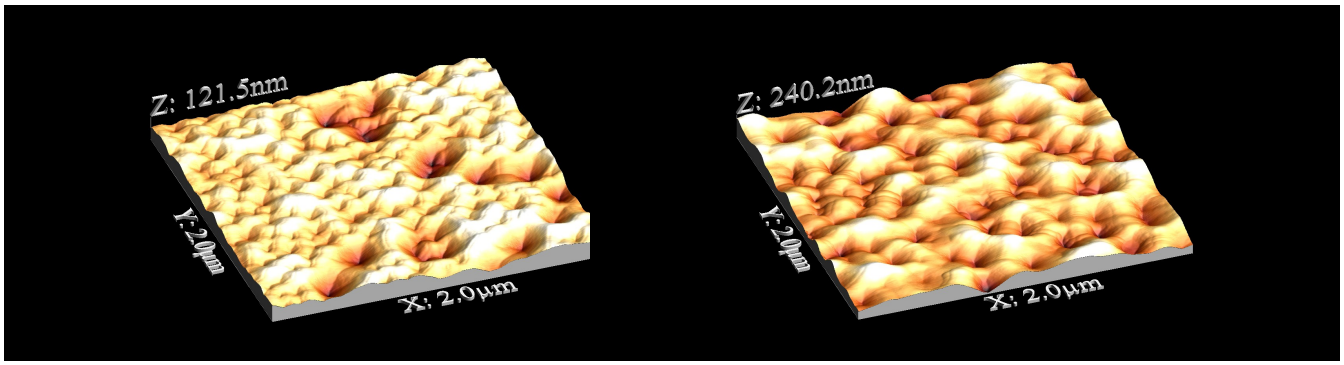

(c) *90W sample.* (d) *110W sample.*

Figure 4.14: Three dimensional AFM images for samples deposited at 50W to 110W. A larger grain size is seen for increasing deposition effects.

Table 4.5: Surface roughness analysis of the power series samples.

Deposition Power (W)	Average roughness (nm)
10	10,1 ± 0,1
20	13,8 ± 0,1
30	13,4 ± 0,7
40	14,4 ± 0,1
50	19,1 ± 0,9
70	14,6 ± 0,1
90	22,4 ± 2,5
110	43,1 ± 1,8

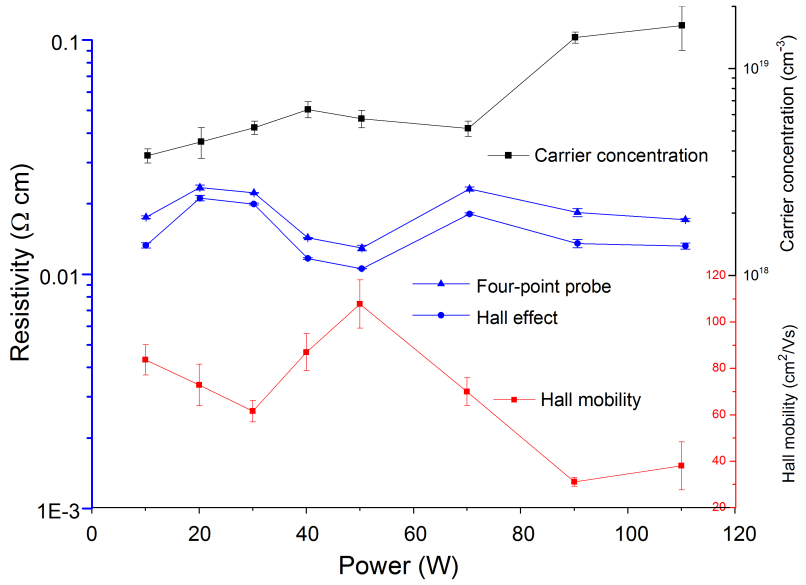

Figure 4.15: *Resistivity measured with both Hall effect and Four-point probe, carrier concentration and Hall mobility plotted as a function of deposition power.*

the PL results a shallow level defect was found to emerge for increasing deposition powers. This shallow level emission peak could originate from interstitial zinc, a donor, and could thus explain the increase in carrier concentration with increasing deposition powers.

The Hall mobility plot does not seem to have a distinct trend. With a higher defect density, the charge carriers experience more scattering events leading to lower mobility. Thus a decrease in mobility for increasing deposition powers would be expected. The mobility of charge carriers also depends on the grain size, i.e. larger grains means fewer grain boundaries which decreases the mobility. The increase in mobility due to larger grains for higher deposition powers, may on the other hand be compensated by the increase in carrier concentration. In particular this applies for the 90W and 110W sample, where the number of excess electrons increases more rapidly compared to the other samples. The maximum in Hall mobility for the 50W sample may be explained by comparing the AFM and PL results. In the near-band edge region of the PL results 4.11, the crystal quality within the grains for the low power samples and the 50W sample deviate to a lower degree than the grain size of the same samples, i.e. the crystal quality is still good, but the grain size increases reducing grain boundary scattering and maximizes the mobility.

The resistivity does not vary much for the different samples. The number of charge carriers increases for higher deposition power, while the mobility has a more decreasing trend. By combining the carrier concentration- and mobility trends, the result is a rather constant resistivity, with a small downfall for the 50W sample, as seen in figure 4.15.

Table 4.6: Roughness analysis of the substrate cleaning series.

Acetone cleaning (minutes)	RMS roughness (nm)
10	12,95
5	1,43
3	2,01
2	1,45
1	2,09

4.3 Temperature dependency

The power series thin films were deposited at 400°C, which is expected to be too low for achieving two-dimensional growth, since the surface mobility of the adatoms sputtered onto the substrate surface may not be sufficiently high for the adatom to find atomic steps on the substrate. From the power series it was found that the 10W deposition gave the best result, but due to the long deposition duration (about 16 hours), the 30W deposition was used for the temperature series. The deposition at 30W power was a good compromise between the quality of the thin film and the duration of the deposition. The 600° deposition duration was 333 minutes. Due to problems with the sputtering system and long periods of down-time, only 600°C was used as deposition temperature (instead of the planned range of temperatures from room temperature to 600°C). Two samples with different pre-cleaning treatments were deposited, with a 15 minutes annealing at 600°C in the sputter chamber before deposition.

After the power series samples were characterized and the AFM pictures analyzed, the substrates and the cleaning procedure was investigated to see why these relatively small grains were obtained. The procedure used for the power series was as mentioned in the sample preparation section (4.1.2), 10 minutes in acetone, 10 minutes in isopropanol and 10 minutes in water, all in ultrasonic bath. The substrates were then dried in nitrogen flow before placed directly in the sputter chamber. ZnO is very reactive and can be damaged by types of all acids, bases and even water. Acetone was expected to be the component of the cleaning process to most likely damage the substrate surface. A cleaning series was therefore done, where the duration of the substrate cleaned in acetone was varied. 5 substrates were cleaned in acetone with different durations: 10, 5, 3, 2 and 1 minute. The substrates were then rinsed in isopropanol and water for 10 minutes each, before dried in nitrogen flow. AFM measurements were done for each of the five samples directly after the cleaning process was finished.

As seen in figure 4.16a and 4.16b there is a significant difference in the z-axis for the substrates washed for 10- and 2 minutes in acetone. The remaining AFM images of the substrate cleaning series can be seen in appendix C, while the measured RMS roughness can be seen in table 4.6. The 196,5 nm height of the 10 minutes substrate may be explained by acetone etching the surface or some layers of acetone remaining on the surface. By comparison of the RMS roughness and the AFM pictures of the different substrates, the substrate washed for two minutes in acetone was determined to be the most suited for deposition.

Unfortunately, the substrate rotation during deposition was out of order, and thus not used. Due to this the thickness of the films could not be measured, since the film on the silicon substrate did not posses a uniform thickness. The deposition procedures were the same as for the power series, albeit with a different deposition temperature, and the deposited

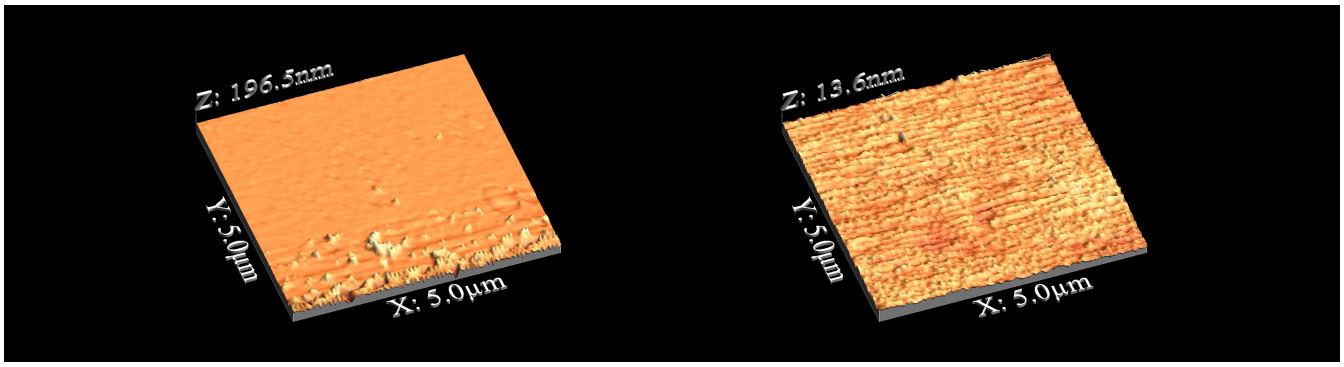

(a) *Substrate cleaned for 10 minutes in acetone.* (b) *Substrate cleaned for 2 minutes in acetone.*

Figure 4.16: Three dimensional AFM images of two of the cleaning series substrates. Measurements done in tuning fork mode.

Table 4.7: Extracted $\theta/2\theta$ scan parameters for the temperature series:

Sample	2θ peak (°)	Std. Err. (°)	FWHM (°)	Std. Err. (°)	Strain	Stress (GPa)
30W 600 °C 2 min acetone	34,427	$8{,}164*10^{-3}$	0,052	$3{,}921*10^{-4}$	$-1{,}842*10^{-4}$	$4{,}291*10^{-2}$
30W 600 °C	34,426	$8{,}101*10^{-3}$	0,049	$2{,}406*10^{-4}$	$-1{,}690*10^{-4}$	$3{,}937*10^{-2}$
30W 400 °C	34,419	$8{,}048*10^{-3}$	0,041	$1{,}556*10^{-4}$	$2{,}964*10^{-5}$	$-6{,}907*10^{-3}$
Substrate	34,424	$8{,}066*10^{-3}$	0,042	$8{,}156*10^{-3}$		

samples was characterized with the same techniques as before.

4.3.1 X-Ray Diffraction

To evaluate the crystal quality of the two samples deposited with 30W power and at 600°C, XRD measurements were done. The substrate used for reference is from a different wafer, but the same batch as the substrates used for the thin film depositions. The scans used were the same as for the power series ($\theta/2\theta$-, Rocking Curve- and ϕ scans). In figure 4.17 the $\theta/2\theta$ scans are presented. From the plot it can be seen that the 30W sample deposited at 600°C has a slightly broader and lower intensity peak than the film deposited at 400°C and 30W, signifying a slightly broader distribution of interplanar spacings. The sample cleaned in acetone for 2 minutes, also shows a slightly broader peak and has an elevation on the left side of the peak. This can be interpreted, as for the power series, as a stress-related peak. The peak position is also shifted a small fraction to the right for both 600°C samples, which means slightly more strain and stress in the film. As before, the elevation of the right hand side stems from the substrate. The $\theta/2\theta$ scan parameters are summarized in table (4.7), where the peak position and FWHM with their respective standard deviations as well as the stresses and strains in the films are presented. It can be seen that the 600°C sample has a larger value for the FWHM and larger absolute value for strain and stress.

The rocking curve scan plots for the two 600°C samples, the 400°C sample and the substrate is shown in figure 4.18. For the sample deposited at 600°C with 2 minutes acetone cleaning, the peak is slightly narrower than for the other 600°C sample, indicating excellent

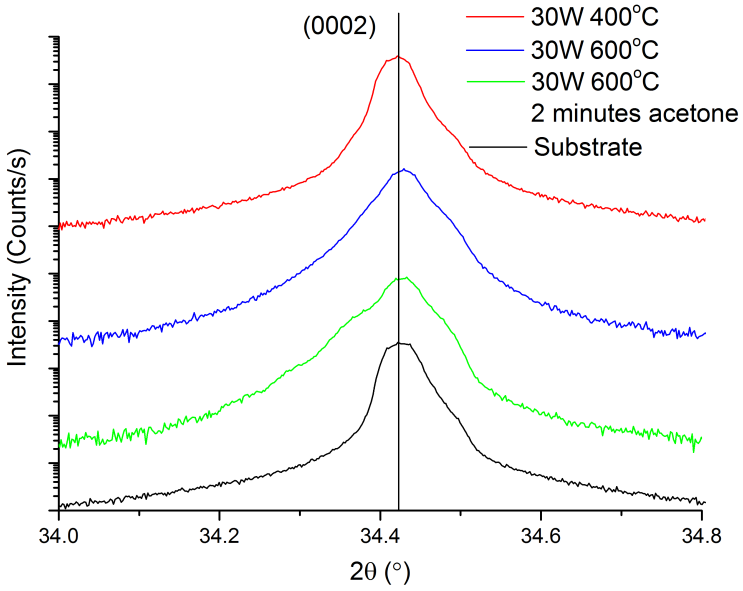

Figure 4.17: *θ/2θ scan of the two 30W samples deposited at 600° C, the 30W sample deposited at 400° C as well as the substrate for reference. The 600° C sample has a slightly broader peak and the peak position is at a slightly higher 2θ value.*

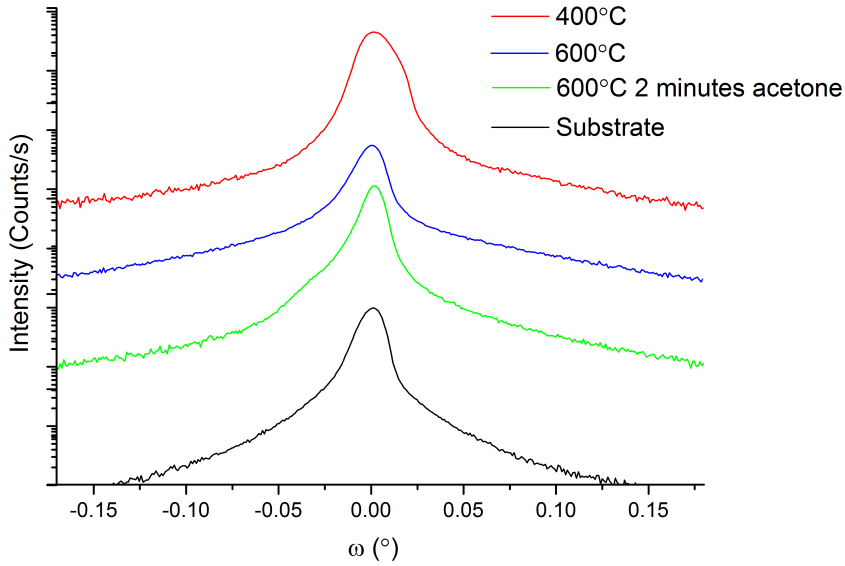

Figure 4.18: *Rocking curve scan for the two 30W 600° C samples, as well as the 30W 400° C sample and the substrate for reference.*

crystal quality with respect to tilted planes and hence screw- and edge dislocations. The rocking curve scan parameters are listed in table (4.8), where it can be seen that the 600°C

Table 4.8: Extracted Rocking Curve scan parameters for the temperature series:

Sample	θ peak (°)	Std. Error (°)	FWHM (°)	Std. Error. (°)
30W 600 ^{0}C, 2 min acetone	17,233	$8{,}045*10^{-3}$	0,010	$1{,}060*10^{-4}$
30W 600 ^{0}C	17,279	$8{,}046*10^{-3}$	0,012	$1{,}098*10^{-4}$
30W 400 ^{0}C	17,224	$2{,}802*10^{-5}$	0,015	$6{,}690*10^{-5}$
Substrate	17,220	$8{,}029*10^{-3}$	0,012	$6{,}866*10^{-5}$

samples have smaller FWHM than the 30W sample deposited at 400°C. The narrower peak for the temperature sample can be interpreted as a smaller concentration of edge- and screw dislocations in the film, which causes tilts in the lattice planes parallel to the surface.

In figure 4.19a and 4.19b the phi scans of the $(10\bar{1}5)$ and $(11\bar{2}4)$ planes of ZnO, respectively are presented. Both scans show six peaks in intervals of approximately 60°, corresponding to the six-fold symmetry of ZnO. Side-peaks are observed in the phi scans of the $(10\bar{1}5)$ plane, meaning some grains in the films have rotational twists with respect to the corresponding plane in the substrate. No major side-peaks are observed for the phi scans of the $(11\bar{2}4)$ plane for the same samples.

4.3.2 Rutherford Backscattering Spectrometry

Rutherford Backscattering Spectrometry (RBS) measurements were made for the thin films deposited at 600°C. The RBS measurements were done by Dr. Alexander Azarov. Figure 4.20 shows the results from both the random- and channeling mode. The thin line show the RBS measurement done in random directions, while the thicker lines at correspond to the RBS/C measurements. The thin film surface can be found at channel number 358, where the surface minimum yield was found to be $\sim$ 8% for both samples, which is higher than for the 30W sample deposited at 400°C ($\sim$2%). For the RBS/C, the thin film cleaned in acetone for 2 minutes yields the lowest number of backscattered ions. This can be interpreted as a lower concentration of defects and impurities present in the crystal channels. The approximately linear slope of backscattered ions as a function of channel number (except for the peak due to oxygen resonance) means that the thin film is indistinguishable from the substrate. For the sample cleaned in acetone for 10 minutes, a change in slope can be observed at approximately channel number 330. Hence, the thin film has higher lattice defects with respect to the substrate since the number of backscattered ions increase more rapidly in the film (above channel 330) compared to the substrate (below channel 330).

4.3.3 Photoluminescence

Photoluminescence (PL) spectroscopy was also employed for the temperature series. The PL measurements were done by Dr. Augustinas Galeckas. Figure 4.21 shows the near-band edge emissions from 3.3 to 3.4 eV, in addition to some other well known emission fingerprints at lower energies. The figure shows the peak at approximately 3.36 eV corresponding to the donor-bound (DX) exciton emission. There is a significant reduction in FWHM of the DX-peak for the samples deposited at 600°C, with respect to the 30W sample deposited at 400°C indicating a higher crystallinity. The intensity of the 600°C sample cleaned for 10 min in acetone shows lower intensity than the sample deposited at 400°C. The sample cleaned for 2 minutes in acetone on the other hand, yields both a lower FWHM and a higher intensity

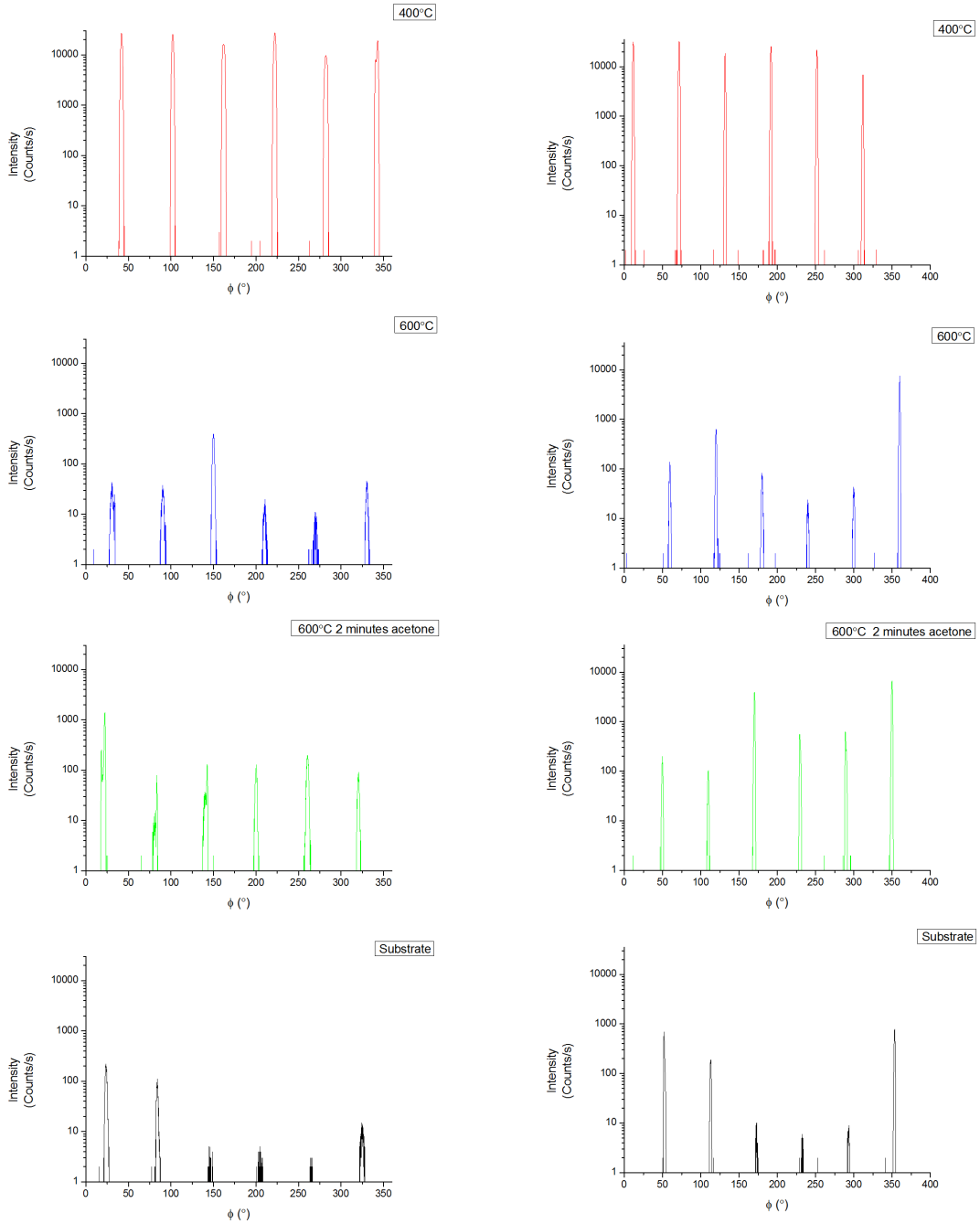

(a) $10\bar{1}5$ ϕ *scan* (b) $11\bar{2}4$ ϕ *scan*

Figure 4.19: ϕ scans of the $(10\bar{1}5)$(a) and $(11\bar{2}4)$ (b) planes of ZnO for the two 30W 600°C samples, as well as the 30W 400°C sample and substrate for reference.

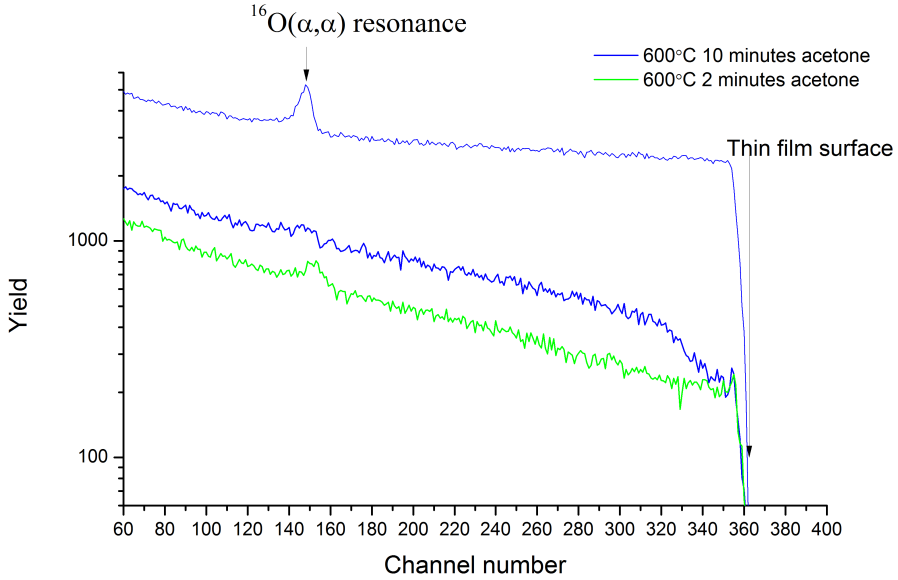

Figure 4.20: *RBS results for the samples deposited at 30W and 600° C. The thick lines show the channeling measurements RBS/C, while the thin line show the measurements done in random mode for the 10 minutes acetone sample and a bulk ZnO sample. The peak observed at approximately channel number 150 is due to oxygen resonance.*

than the sample deposited at 400°C. This means that fewer defects are contributing to the emission which again points towards higher crystal quality. In contrast to the 30W 400°C sample, three well distinct peaks can be observed for both samples deposited at 600°C to the right of the DX-peak. The emission peaks observed in the spectrum at $\sim$ 3.32, $\sim$ 3.29 eV and $\sim$ 3.22 eV are often appointed to the two-electron satellite (TES) and the donor-bound excitons coupled to longitudinal optical phonons (DX-LO and DX-2LO), respectively. The donor-bound longitudinal optical phonon emission peak, is an emission level for the donor-bound exciton. The recombination of this exciton will thus emit a phonon, lowering the exciton energy by a fraction before emitting a photon. For the next level (DX-2LO), two phonons are emitted prior to full relaxation through photon emission. Thus the energy difference between each of the three peaks (DX, DX-LO and DX-2LO) corresponds to the energy of one phonon ($\sim$ 0.07 eV). The peaks are more distinct for the sample cleaned for 2 minutes in acetone than the other 600°C sample. The fact that these peaks are observable, in contrast to the power series samples, can again be interpreted as higher crystal quality. For the wider energy spectrum showing the deep level emissions, as shown in figure 4.22, the 600°C sample has a higher intensity for the deep level defects at 2-2.5 eV. The 30W (2 minutes acetone) sample yields the highest intensity for this defect, which, as mentioned previously may originate from O_i or V_O. The shallow level defect at about 3 eV seen for higher sputtering powers samples, is not observable in any of the 30W samples.

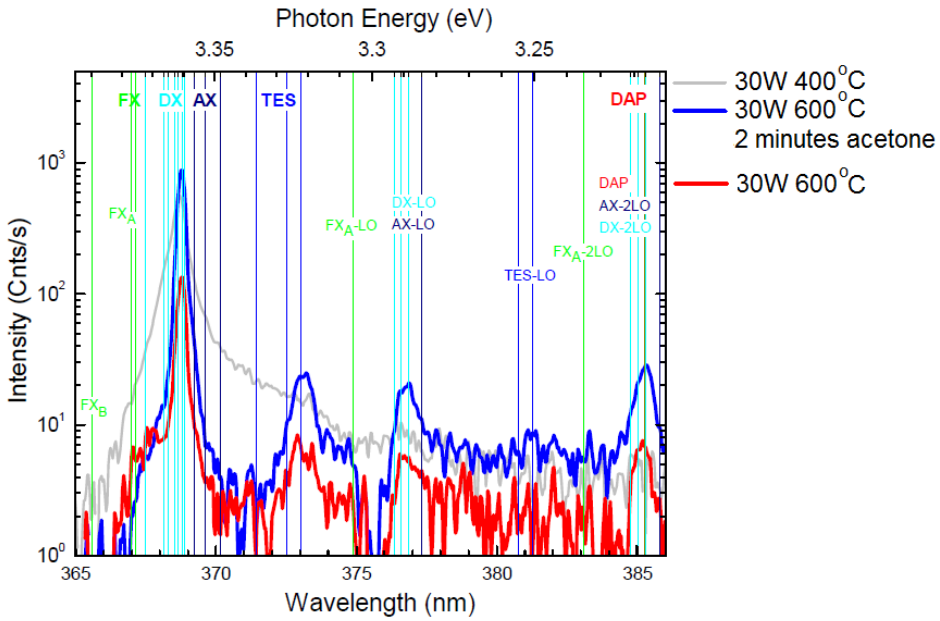

Figure 4.21: *Near-band edge PL emissions for the temperature series.*

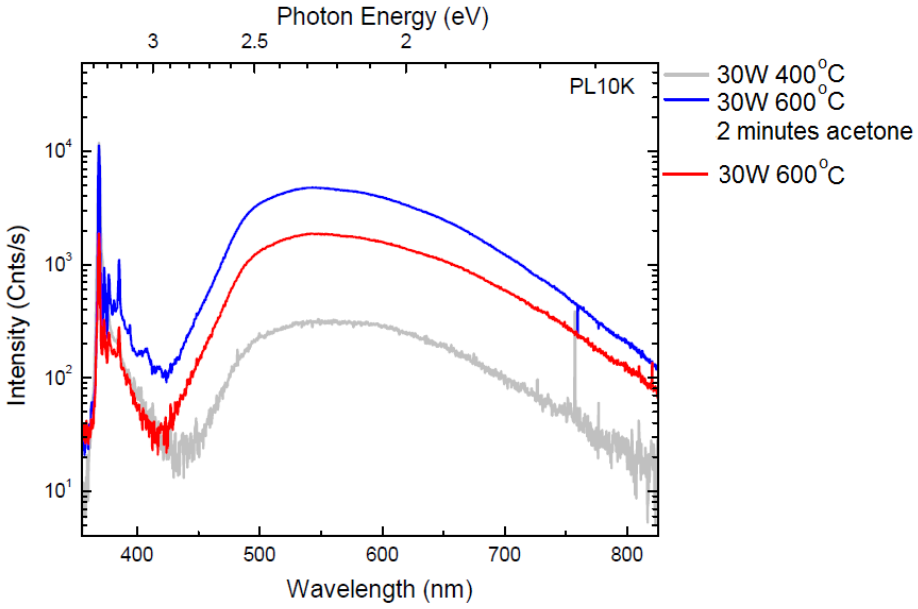

Figure 4.22: *PL measurements displaying a broad spectrum to visualize shallow- and deep level defects.*

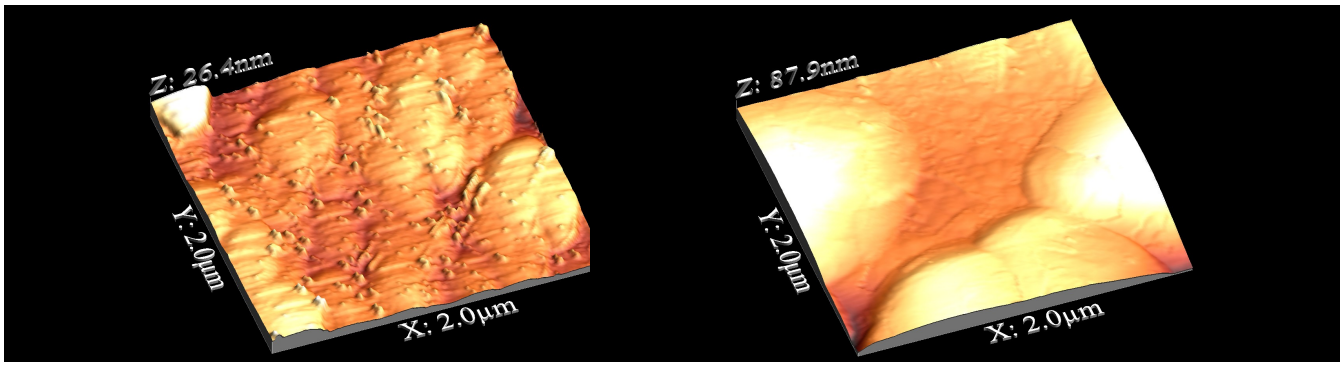

(a) *30W 600°C sample.* (b) *30W 600°C, 2 minutes acetone.*

Figure 4.23: Three dimensional AFM images of samples deposited with 30W at 600°C.

Table 4.9: Surface roughness analysis of the temperature series samples.

Deposition Temperature (°C)	Average roughness (nm)
600, 2 min acetone	12,8 ± 9,6
600	3,4 ± 0,3
400	13,4 ± 0,7

4.3.4 Atomic Force Microscopy

AFM tapping mode measurements were made on the two samples deposited at 600°C, and can be seen in figure 4.23a and 4.23b. Surface roughness was expected to decrease with increasing deposition temperature, due to the higher surface mobility of the adatoms. The higher mobility then gives the adatoms a higher probability of finding the most energetically favorable place. Comparing the 600°C samples with the 30W sample deposited at 400°C, reveals a flatter surface, most easily seen using the z-axis in the pictures (26.4 nm for 30W 600 °C and 100.7 nm for 400 °, both cleaned for 10 minutes in acetone and 87.9 nm for the sample cleaned for 2 minutes in acetone). The most obvious difference between the samples deposited at 600 °C and 400 °C is the grain size. In figure 4.23a the 600 °C sample cleaned for 10 minutes in acetone can be seen to have dust particles on the surface, but underneath these, larger grains are observed. The sample cleaned for 2 minutes in acetone possesses even larger grains. Although larger grains was accomplished with deposition at 600 °C, two-dimensional growth has not been accomplished. In table (4.9) the surface roughness analysis of the 600°C samples is shown, with the 30W sample deposited at 400°C as a reference. From the AFM measurements larger grains are observed, but less surface roughness was obtained for the 30W, 600°C, 10 minutes acetone sample. The sample cleaned for two minutes in acetone, had an unexpected relatively higher roughness compared to the sample cleaned for 10 minutes in acetone. Larger grains are however observed, meaning larger areas were grown epitaxially.

4.3.5 Hall Effect Measurements

The resistivity, Hall mobility and carrier concentration was measured by Hall effect measurements, while the resistivity was also measured using the four-point probe. The carrier

Table 4.10: Hall mobility and carrier concentration measured for the temperature series. The sample cleaned for 2 minutes in acetone is excluded from this table.

Temperature (°C)	Hall mobility (cm^2/Vs)	Carrier concentration (cm^{-3})
600	3,36 ± 1,41	1,58 ± 1,08 *10^{19}
400	61,57 ± 4,58	5,78 ± 0,43 *10^{18}

Table 4.11: Temperature series resistivity measured with Hall effect and Four-point Probe.

	Hall Effect Measurements	Four-point Probe
Temperature (°C)	Resistivity (Ω cm)	Resistivity (Ω cm)
600, 2 min acetone	5,38 ± 2,31	4,70 ± 0,45
600	0,68 ± 0,068	0,29 ± 0,04
400	0,02 ± 1,74*10^{-4}	0,02 ± 6,16*10^{-5}

concentrations and Hall mobilities are shown in table (4.10). The lower Hall mobility for the 600° cleaned for 10 minutes in acetone is difficult to explain. The larger grains seen from the AFM measurements and the lower defect concentration seen from the PL measurements, makes the lower mobility unexpected. For the sample cleaned for 2 minutes in acetone, the decrease of four orders of magnitude in carrier concentration and the two orders of magnitude increase in mobility makes the results rather unlikely. The size of the sample is so small that contacting with the van der Pauw setup was difficult, which may be one reason for the rather unlikely results. In table (4.11) the resistivities measured with the two different methods are shown. The table shows a increase in resistivity for the samples deposited at 600°C. The sample cleaned in acetone for 2 minutes possesses the highest resistivity, but the trends are difficult to correlate to the structural and optical properties of the sample.

Chapter 5

Discussion

5.1 Power Series

In this study it was found that higher crystal quality of ZnO films was obtained at lower sputtering deposition power. $\theta/2\theta$ scans evidenced side peaks corresponding to strain and stress emerging for increasing deposition powers. This may be due to surface damage on the substrate and thin film during growth. At higher deposition powers the sputtered atoms and molecules posses a larger amount of energy when hitting the substrate- and thin film surface, which can cause surface damage. The relatively low substrate temperature is not sufficient to repair this damage. The films also showed a three-dimensional growth, i.e. islands or grains that grows individually and not layer on layer, which can also be explained by the low substrate temperature during deposition, giving the sputtered adatoms lower mobilities and hence lower probabilities of finding the most energetically favorable place. The trend of smaller grains for lower deposition powers is likely due to the combination of low energy when hitting the substrate surface and the relatively low substrate temperature, yielding low surface mobility. The lack of 2D growth can also be explained by possible defects or irregularities on the substrate surface, acting as templates for parts of the thin film growth.

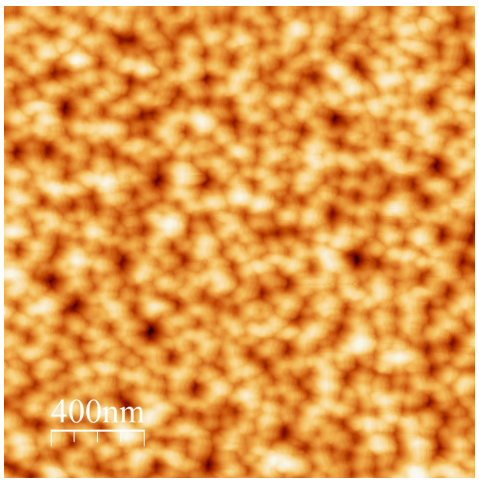

Figure 5.1: *Two-dimensional AFM image of the 10W sample.*

These potential irregularities could be incorporated during the cleaning of the substrate.

Homoepitaxial growth, where the thin film and substrate are indistinguishable, demands perfect substrate surfaces.

The grain formation during deposition, i.e. island growth, is able to explain the side-peaks observed in the ϕ scans. Since there are grains, there must be grain boundaries and these grain boundaries arises because of a small rotational twist between the individual grains. These rotated grains from the thin films, give rise to the side-peaks observed in the ϕ scans.

The dislocation concentration was found to increase with increasing deposition powers, while the RBS/C result showed a very low yield of backscattered ions for the low power samples. The channels within the crystal structure thus contain a low concentration of defects or impurities which would increase the number of scattering events. The PL near-band edge emission spectrum also showed a distinct DX-peak for the low power samples, supporting the RBS/C results in that the defect- and impurity concentrations are lower for the low power samples. The decreasing XRD FWHM for decreasing deposition power has also been reported by Kim et.al. [31]. The 90W and 110W thin films RBS/C yields are distinguishable from the substrate RBS/C yields and the yield of backscattered ions are significantly higher. By comparing this result to the almost absent peak in the near-band edge emission PL spectra, the films of these higher deposition powers can be understood to contain a higher concentration of defects and impurities. The Hall effect measurements also yields a high carrier concentration for all samples, which may be caused by a higher number of defects acting as donors. The high carrier concentration can thus be explained by the high concentration of Al in the films found by SIMS measurements. The Al atoms substitute for Zn and thus acts as donors [58]. Although relatively low concentrations of Li were found in the films, especially for the low effect samples, if placed on interstitial sites Li also act as a donor [15].

The AFM measurements of the power series samples showed decreasing roughness for decreasing deposition powers. The 2D pictures of the samples are shown in figures 5.1, 5.2a and 5.2b for the 10W, 50W and 110W sample respectively. The grain size was also found to

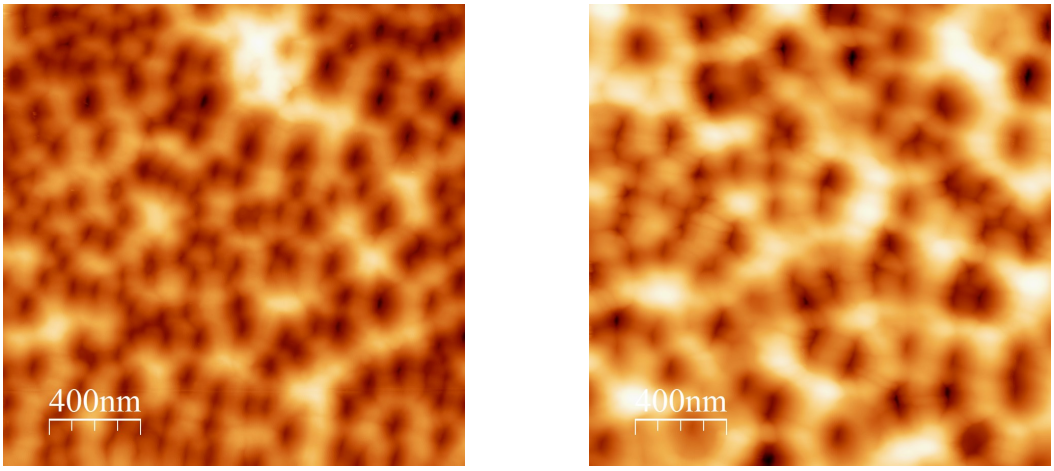

(a) *50W* (b) *110W*

Figure 5.2: Two-dimensional AFM images. A hexagonal ordering of grains can be seen.

be decreasing for decreasing deposition effects. Some of these grains can be seen to posses a hexagonal ordering with respect to each other. This becomes more evident for higher deposition effects, where the number of grains is lower and the grain size is larger. For both

the 50W and 110W sample more distinct hexagonal ordering of the grains is observed. This points towards a mechanism where the atoms and molecules during deposition nucleate at the lattice points of the substrate.

With all this in mind, the two-dimensional epitaxial growth has not been obtained. The excellent crystal quality and relatively low impurity concentration for the 10W and 30W sample however, point to a local homoepitaxial growth in the c-direction.

5.2 Temperature dependency

The promising power series results gave expectations of even better results for the samples deposited at higher temperature. In this section only the temperature series sample cleaned the same way as the power series (10 minutes in acetone) is discussed. The $\theta/2\theta$ result showed a slightly broader peak (FWHM of 0,049°) than the 30W sample deposited at 400°C (FWHM of 0.041°). The increase in FWHM for the $\theta/2\theta$ scan may be explained by the lack of rotation during deposition. Since the substrate did not rotate and the target material has an angle with respect to the substrate holder, the side of the substrate closest to the target material could obtain more damage during deposition. The increase in stress and strain for the temperature sample is though very small. The RBS/C also show a decrease in crystal quality for the 600°C sample. The narrower peak in the rocking curve scan, with FWHM of 0.012° for the 600°C sample and FWHM of 0.015° for the 400°C sample, evidences a lower concentrations of dislocations and especially screw- and edge dislocations which causes tilts in the crystal planes nearly parallel to the surface. The ϕ scan showed some side-peaks which as for the power series can be explained by the rotational twist of some volumes (grains) with respect to the rest. The high crystal quality extracted from the XRD results are supported by the photoluminescence spectra in the near-band edge emission region. The very distinct peak corresponding to the donor-bound exciton emission, indicates that few other defects contribute to the carrier recombination. Like for the power series, the elevations on the left hand side of this distinct peak corresponds to the free-exciton emission, which points towards high crystal quality. The fact that the DX-LO and DX-2LO emission peaks are distinguishable from noise, which is not possible for the power series samples can be interpreted as excellent crystal quality. In addition, like Furusawa et.al. [32], the peak corresponding the two-electron satelite (TES) at 3.32 eV is observable. Since this is a radiative electronic transition involving an excited state of a donor, it can only be observed in films of high crystal quality with long coherence length. The DX-LO and DX-2LO replicas are also observable for the temperature sample and not the power series sample and are due to low concentrations of non-radiative emissions. This can be explained by the larger grains observed in the AFM measurements.

The AFM pictures showed larger grains than for the power series, as seen in figure 5.3a and 5.3b, which is an indication of higher surface mobility of the sputtered adatoms. The larger grains for higher substrate temperature has also been reported by Bikowski et.al. [59], and is the result of a higher concentration of point defects being annealed out during deposition. As fewer point defects are present, a decrease in lattice expansion and thus an increase in crystallites sizes are obtained. The thin film surface also show a significant decrease in surface roughness. As for defects and impurities, there is an increase in carrier concentration for the samples deposited at 600°C. The PL results show no signs of higher impurity concentrations which can contribute excess electrons, i.e. shallow donors. The deep level defect seen in the wide emission spectra of the PL results 4.22 yields a higher intensity for the 600°C sample,

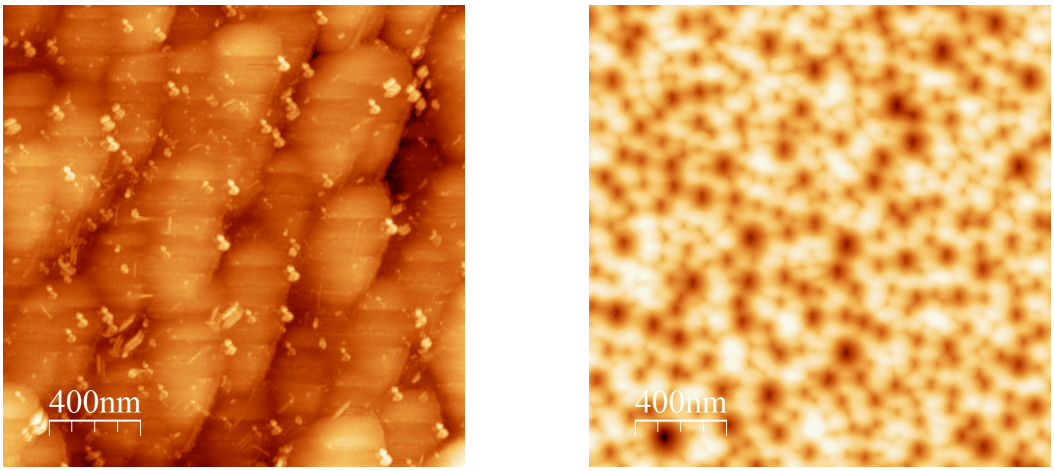

(a) *30W sample deposited at 600° C* (b) *30W sample deposited at 400° C.*

Figure 5.3: Two-dimensional AFM figures of the 30W samples deposited at different temperatures. A significant increase in grain size is observable for the sample deposited at 600°C.

but due to its deep position in the band gap will not contribute carriers. The unintentional incorporation of hydrogen might be one explanation, but other unintentional incorporated impurities may also contribute to the higher carrier concentration as for example Li which if place on interstitial site act as a donor, or Al which both was found present in the power series thin films, which points towards the presence of these also in the 600°C samples.

The significantly lower Hall mobility for the temperature sample is somewhat of a mystery. Ellmer et.al [60] reported that for ZnO with carrier concentrations up to 10^{20} cm^{-3} the mobility is mainly limited by grain boundary scattering. The temperature sample shows significantly larger grains compared to the 400°C sample, thus the lower mobility may be due to a ionized impurity scattering, because of the high carrier concentration.

Due to the lack of rotation during the deposition a thickness gradient may be present for the temperature samples. A thickness gradient in the film results in a carrier concentration gradient. This carrier concentration gradient means that if current is injected in the high concentration area and leaves in the low concentration area, the carrier concentration gradient works with the current. This is because diffusion always goes from high- to low concentration. For the reverse case, the gradient works against the current. The result is that the thickness gradient in the film may be the answer to the higher resistivity and lower mobility of the sample deposited at 600°C. As for the low effect power series samples, the 600°C samples showed high crystallinity within the grains. Therefore due to the larger grains, larger areas of the surface were grown with greater crystal quality. By further increasing the substrate temperature during deposition, two-dimensional growth might be achievable [31].

5.3 Substrate Cleaning

In this section, the samples deposited at 600°C cleaned in acetone for 10- and 2 minutes will be referred to as the 2 minutes- and 10 minutes sample, respectively. The $\theta/2\theta$ scan showed an evident stress-related side-peak for the 2 minutes sample, which is not clear for the 10 minutes sample. This may also be explained by the lack of rotation during deposition, as explained

in the discussion for the temperature dependency. A higher FWHM value of 0.052° for the 2 minutes sample is also observed, compared to the FWHM value of 0.049° for the 10 minutes sample pointing towards a lower crystal quality. The rocking curve results on the other hand states that a lower number of planes nearly parallel to the surface contains a tilt in the 2 minute sample, since it has a lower rocking curve FWHM (0.010° for the 2 minutes sample and 0.012° for the 10 minutes sample). As for the power- and temperature series, the side-peaks in the ϕ scan results arises from the rotational twist of grains, since grain boundaries arise when grains in the film are grown with a small rotation with respect to the rest. The $\theta/2\theta$ scan on the other hand shows a decrease in crystal quality in the c-direction. The RBS/C yield is also lower for the 2 minute sample compared to the 10 minutes sample. The PL results show an increase in crystal quality for the 2 minutes sample. Both samples shows a narrow peak corresponding to the donor-bound exciton, but the 2 minutes sample has a higher intensity. This in addition to the more distinct peaks of the LO replicas (DX-LO and DX-2LO), can be interpreted as a lower concentration of defects and impurities and points towards higher a crystal quality. The PL results are consistent with the AFM data as the larger grain size implies less grain boundaries giving rise to non-radiative recombination centers. By comparing the XRD and PL results there has been an increase in crystal quality. However, the $\theta/2\theta$ scan suggest more stress and strain. The grains are also larger for the 2 minutes sample, but with more surface roughness. The emission at 2-2.5 eV in the PL results, corresponding to deep level defects is higher for the 2 minutes sample, suggesting more incorporation of deep defects.

By comparing the XRD and PL results higher crystal quality has been obtained by cleaning with 2 minutes acetone instead of 10 minutes. As for the low effect power series- and temperature samples epitaxial growth has been achieved in the grains. For the 2 minutes sample the grains are larger than for the 10 minutes sample, which means that the change in pre-cleaning procedure has resulted in thin films with growth close to two-dimensional growth.

Chapter 6

Conclusion

6.1 Summary

Homoepitaxial growth of ZnO was achieved within individual c-axis oriented columnar grains using sputter deposition. Lower deposition power gave higher crystal quality within the grains, but the grain size decreased. XRD revealed a very low magnitude of strains and stresses, no tilts in the planes nearly parallel to the surface and hence a very low concentration of edge- and screw dislocations. The grains were found to posses a small rotational twist with respect to each other. The high crystal quality for lower deposition power found with XRD is consistent with both RBS/C and PL results. RBS/C showed lower yields with decreasing deposition power, and the thin films were not distinguishable from the substrates for the low power samples. The PL results revealed a lower concentration of defects contributing to non-radiative recombinations in the near-band edge region, while an emerging peak related to deep level emissions pointed toward higher incorporation of deep level defects for the low power samples. The high carrier concentration of the thin films was found to be due to Al incorporation during growth. Due to lower adatom surface mobility, a decrease in grain size was observed at decreasing deposition powers, and hexagonal grain ordering was observed.

Higher deposition temperature (600°C) resulted in significantly larger grains, due to higher adatom surface mobility. The XRD $\theta/2\theta$ scan and RBS/C showed a decrease in crystal quality in forms of more strain and stress and higher backscattering yield, respectively, compared to the same deposition power at 400°C. XRD rocking curve-, PL- and AFM results on the other hand pointed to higher crystal quality, especially for the sample cleaned in acetone for 2 minutes. The lowest value of the XRD rocking curve FWHM (0.010°) was achieved with deposition at 30W, 600°C and 2 minutes acetone cleaning. PL showed higher intensity and smaller FWHM of the DX-peak in the near-band edge region, while peaks corresponding to TES, DX-LO and DX-2LO was observed, all pointing towards less defects contributing to non-radiative recombinations and hence higher crystal quality. A change in substrate cleaning procedure gave an increase in both crystal quality and grain size, according to XRD rocking curve, RBS/C, PL and AFM.

6.2 Suggestions for further research

For obtaining two-dimensional homoepitaxial growth using sputter deposition, higher deposition temperature is probably needed. In this study, it was found that the maximum deposition

temperature of 600°C most likely is the limitation to why two-dimensional growth was not achieved, although the maximum temperature gave relative large grains. By further increasing the temperature, the increased adatom surface mobility will result in larger grains, or even a single crystal.

The next step for optimizing growth conditions, after optimization of both deposition-power and temperature, can be characterizing the effects of varying gas flow during deposition. By optimizing the gas flow, using maximum deposition temperature and the deposition power yielding the highest crystal quality, the three most important parameters for growth conditions using sputter deposition would be optimized.

A deeper investigation into the substrate cleaning procedure could also increase the substrate surface quality, and hence give better conditions for two-dimensional growth. By reducing the substrate acetone cleaning by only 8 minutes, a significant increase in both crystal quality and grain size was observed, so an optimization of the pre-deposition cleaning of the substrates would increase the probability of two-dimensional growth of ZnO by sputter deposition.

Appendix A

Power Series at Higher Chamber Pressure

An initial power series was made before the chamber pressure was reduced. The films were deposited at highly resistive ZnO substrates purchased from Tokyo Denpa, grown by the hydrothermal method. The gas flow was 70 sccm Ar, substrate temperature was 400°C, the chamber pressure was 21.5 mTorr and the samples was rotated with 11 rpm. 10 minutes presputtering was done to remove impurities in the target material. The deposition powers were the same; 10W, 20W, 30W, 40W, 50W, 70W, 90W and 110W.

The $\theta/2\theta$ scans in figure A.1 shows major side peaks for the high power samples, which means a large amount of stress and strain in the films. These films thus yields poor crystal quality, and have not been grown epitaxially. For the low power samples (10W and 20W) only one side peak, possibly originating from the substrate can be observed. For the rocking curve scans the 10W sample gave the lowest FWHM value, which can be seen in table (A.1).

The FWHM results from the rocking curve scans is higher than for those discussed in the thesis (see table (4.3)). As for the power series deposited at 7 mTorr, the 10W sample yields the best crystal quality. The $\theta/2\theta$ results shows that the film- and substrate mismatch occurs at lower deposition powers in the study using a chamber pressure of 21.5 mTorr, than for the power series deposited at lower chamber pressure. Based on these results, in addition to AFM measurements, PL measurements and Hall measurements, it was decided to reduce the chamber pressure and make a new power series.

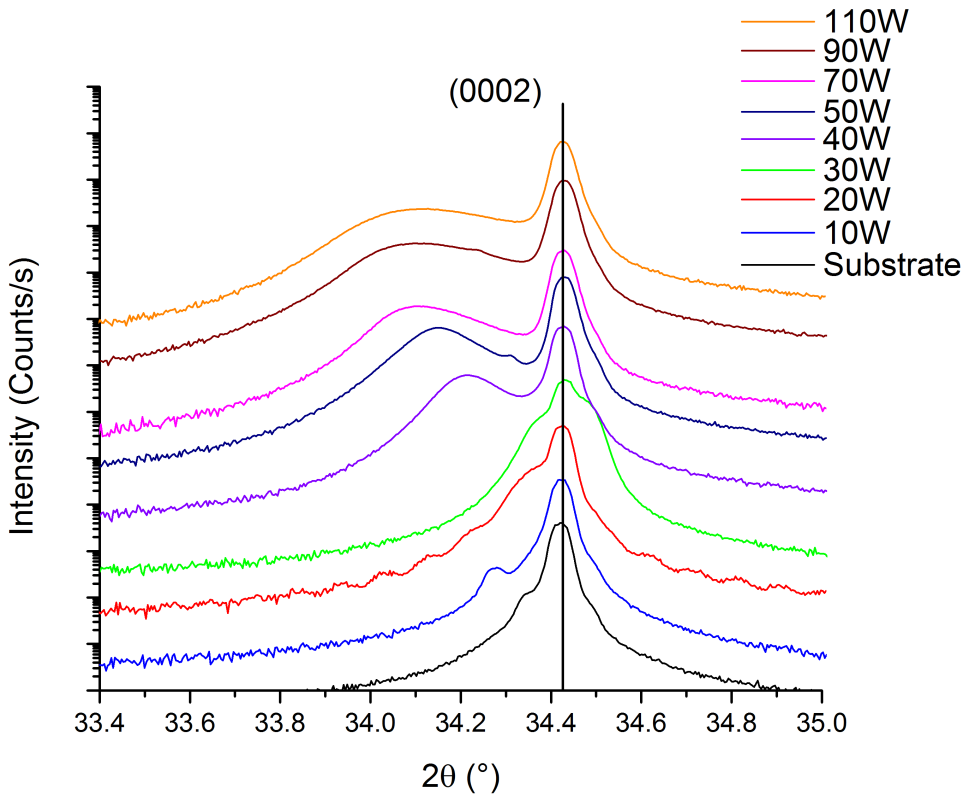

Figure A.1: *θ/2θ scan for the power series deposited at high chamber pressure.*

Table A.1: Extracted rocking curve FWHM for the power series samples deposited at high chamber pressure, where the instrumental broadening has been taken into account.

Deposition effect (W)	FWHM (°)
Substrate	0.013
10	0.015
20	0.015
30	0.017
40	0.023
50	0.029
70	0.034
90	0.038
110	0.037

Appendix B

Angle Series for Magnetron Sputter

A series of depositions of ZnO on silicon wafers were done to investigate the target angle dependency of the thin film uniformity. By varying the target angle with respect to the substrate holder, different thickness uniformities were found for the deposited thin films. For all depositions the power was 50W, the gas flow was 70 sccm Ar, the chamber pressure during deposition was 17.0 mTorr, the substrate temperature was 400°C and the substrates were rotated with 11 rpm. 10 minutes presputter was done, to remove impurities in the target material before the deposition was started. In the sputter chamber, the angle is represented as lines. Line number zero places the target parallel with the substrate surface normal. Each line represents about 4°, so by aligning the target at line 4,5 gives an angle of $\sim 18°$ to the substrate surface normal. The first eight depositions were done with a distance between target and substrate holder of 11 cm, as seen in figures B.1a-B.1d and B.2a-B.2d.

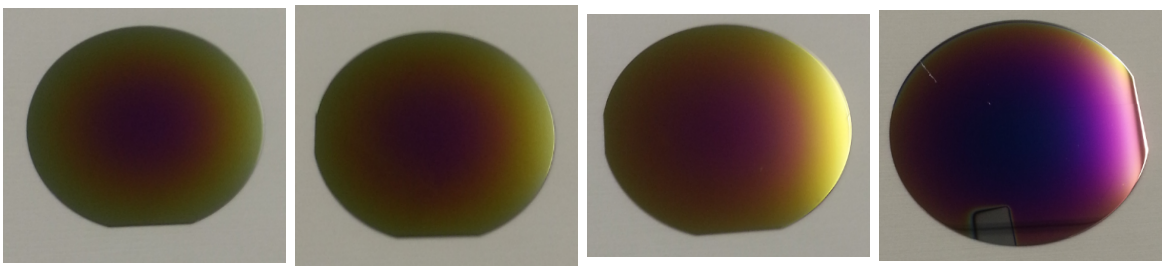

(a) *30°* (b) *28°* (c) *26°* (d) *24°*

Figure B.1: Angle series with target the 11 cm from the substrate holder.

The thickness uniformity can clearly be seen to be angle dependent, and ∼18° was found to give the best result, due to the lowest color gradient from the center to the wafer edges. The target-to-substrate holder distance was then reduced to 10 cm. A new series was deposited with a target angle of 16°, 18°, 20° and 22°. 18° also gave the best result for this series. The conclusion of this angle series was to set the target with a 10 cm distance and an angle of ∼18°.

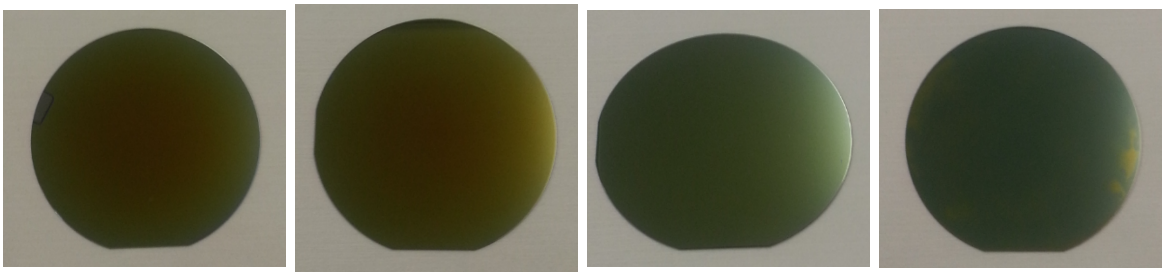

(a) *22°* (b) *20°* (c) *18°* (d) *16°*

Figure B.2: Angle series with the target 11 cm from the substrate holder.

Appendix C

AFM Images for Substrate Cleaning Series

A cleaning series was done where the duration of acetone cleaning was varied, as mentioned in section 4.3. The different acetone cleaning durations were 10 minutes, 5 minutes, 3 minutes, 2 minutes and 1 minute. The substrates were then rinsed in isopropanol and water for 10 minutes each, before dried in nitrogen flow. The AFM measurements done for the substrate cleaning series were done immediately after cleaning using tuning fork mode. As seen in figure C.1a-C.1b, C.2a-C.2b and C.3 the height (z-scale) decreases for reduction in acetone cleaning duration, possibly due to a reduction in the concentration of acetone residues on the substrate surface. The substrate cleaned in acetone for 2 minutes yields the best surface, while for the substrate cleaned for 1 minute surface peaks possibly corresponding to dust particles are observed, resulting in an increase in z-axis height.

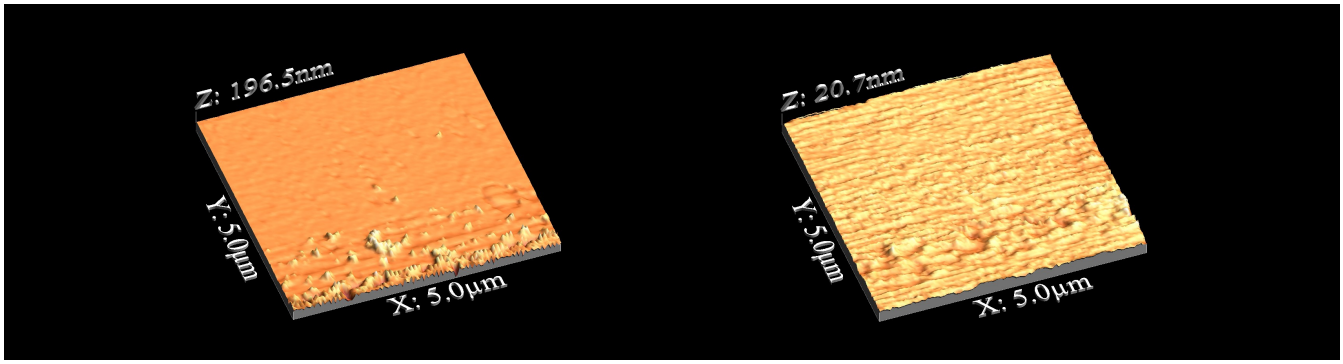

(a) *Substrate cleaned for 10 minutes in acetone.* (b) *Substrate cleaned for 5 minutes in acetone.*

Figure C.1: Three dimensional AFM images of two of the cleaning series substrates.

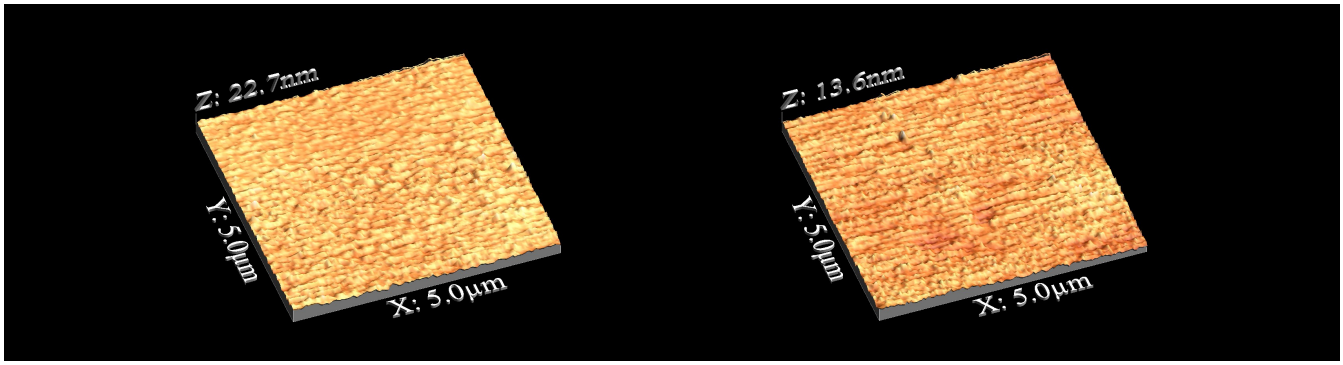

(a) *Substrate cleaned for 3 minutes in acetone.* (b) *Substrate cleaned for 2 minutes in acetone.*

Figure C.2: Three dimensional AFM images of two of the cleaning series substrates.

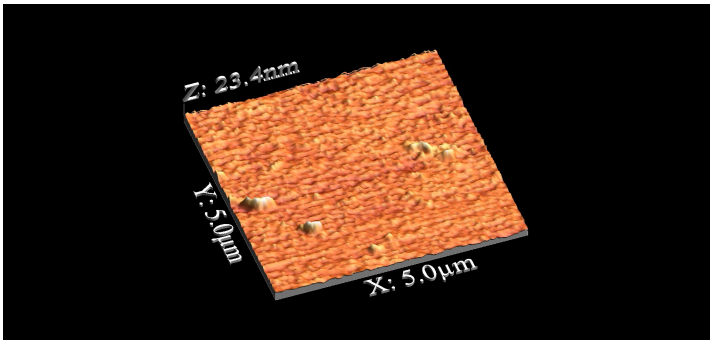

Figure C.3: *Three dimensional AFM image of the substrate cleaned for 1 minute in acetone.*

Bibliography

[1] International Energy Agency, *Technology Roadmap - Solar Photovoltaic Energy*. International Energy Agency, 2014 ed., 2014.

[2] T. International Zinc Association, "Zinc... A Sustainable Material," 2010.

[3] W. Li, C. Kong, G. Qin, H. Ruan, and L. Fang, "p-Type conductivity and stability of Ag-N codoped ZnO thin films," *Journal of Alloys and Compounds*, vol. 609, pp. 173 – 177, 2014.

[4] T. N. Xu, X. Li, Z. Lu, Y. Y. Chen, C. H. Sui, and H. Z. Wu, "Realization of Ag-S codoped p-type ZnO thin films," *Applied Surface Science*, vol. 316, pp. 62 – 65, 2014.

[5] R. Triboulet and J. Perrière, "Epitaxial growth of ZnO films," *Progress in Crystal Growth and Characterization of Materials*, vol. 47, no. 2-3, pp. 65 – 138, 2003. Vapour Growth of Bulk Crystals and Epitaxy: Part I Vapour Growth of Bulk Crystals and Epitaxy: Part I.

[6] B. G. Streetman and S. K. Banerjee, *Solid State Electronic Devices*. Pearson Prentice Hall, 6 ed., 2006.

[7] R. J. D. Tilley, *Understanding Solids - The Science of Materials*. John Wiley & Sons, LTD, 2004.

[8] U. Müller, *Inorganic Structural Chemistry*. John Wiley & Sons, LTD, 2. ed., 2007.

[9] C. Kittel, *Introduction to Solid State Physics*. John Wiley & Sons, Inc., 7 ed., 1996.

[10] P. C. Hemmer, *Faste Stoffers Fysikk*. Tapir Forlag, 1987.

[11] D. J. Griffiths, *Introduction to Quantum Mechanics*. Pearson Prentice Hall, 2 ed., 2005.

[12] J. A. Venables, *Introduction to Surface and Thin Film Processes*. Cambridge University Press, 2003 ed., 2000.

[13] S. A. Campbell, *Fabrication Engineering at the micro- and nanoscale*. Oxford University Press, 3 ed., 2008.

[14] R. B. Heller, J. McGannon, and A. H. Weber, "Precision determination of the lattice constants of zinc oxide," *J. Appl. Phys.*, vol. 21, no. 12, pp. 1283–1284, 1950.

[15] Ü. Özgür, Y. I. Alivov, C. Liu, A. Teke, M. A. Reshchikov, S. Dogan, V. Avrutin, S. J. Cho, and H. Morkoc, "A comprehensive review of ZnO materials and devices," *J. Appl. Phys.*, vol. 98, 2005.

[16] K. Momma and F. Izumi, "VESTA 3 for three-dimensional visualization of crystal, volumetric and morphology data," *J. Appl. Crystallogr.*, vol. 44, pp. 1272–1276, Dec 2011.

[17] A. F. Kohan, G. Ceder, D. Morgan, and C. G. Van de Walle, "First-principles study of native point defects in ZnO," *Phys. Rev. B*, vol. 61, pp. 15019–15027, Jun 2000.

[18] A. Janotti and C. G. Van de Walle, "Native point defect in ZnO," *Phys. Rev. B*, vol. 76, October 2007.

[19] C. G. Van de Walle, "Defect analysis and engineering in ZnO," *Physica B: Condensed Matter*, vol. 308-310, pp. 899 – 903, 2001. International Conference on Defects in Semiconductors.

[20] J. I. Owen, *Growth, Etching, and Stability of Sputtered ZnO:Al for Thin-Film Silicon Solar Cells*, vol. 125. Forschungszentrum Jülich GmbH, 2011.

[21] C. G. Van de Walle, "Hydrogen as a Cause of Doping in Zinc Oxide," *Phys Rev Lett*, vol. 85, pp. 1012–1015, Jul 2000.

[22] W. Walukiewicz, "Defect formation and diffusion in heavily doped semiconductors," *Phys. Rev. B*, vol. 50, no. 8, 1994.

[23] J. C. Fan, K. M. Sreekanth, Z. Xie, S. L. Chang, and K. V. Rao, "p-type ZnO materials: Theory, growth, properties and devices," *Progress in Materials Science*, vol. 58, no. 6, pp. 874 – 985, 2013.

[24] E. C. Lee, Y. S. Kim, Y. G. Jin, and K. J. Chang, "Compensation mechanism for N acceptors in ZnO," *Phys. Rev. B*, vol. 64, p. 085120, Aug 2001.

[25] A. Tsukazaki, A. Ohtomo, T. Onuma, M. Ohtani, T. Makino, M. Sumiya, K. Ohtani, S. F. Chichibu, S. Fuke, Y. Segawa, H. Ohno, H. Koinuma, and M. Kawasaki, "Repeated temperature modulation epitaxy for p-type doping and light-emitting diode based on ZnO," *Nat. Mater.*, vol. 4, no. 1, pp. 42–46, 2005.

[26] S. Chu, J. H. Lim, L. J. Mandalapu, Z. Yang, L. Li, and J. L. Liu, "Sb-doped p-ZnO / Ga-doped n-ZnO homojunction ultraviolet light emitting diodes," *Appl. Phys. Lett.*, vol. 92, no. 15, pp. –, 2008.

[27] H. Liu, V. Avrutin, N. Izyumskaya, Ü. Özgür, and H. Morkoc, "Transparent conducting oxides for electrode applications in light emitting and absorbing devices," *Superlattices Microstruct*, vol. 48, no. 5, pp. 458 – 484, 2010.

[28] S.-M. Park, T. Ikegami, and K. Ebihara, "Effect of substrate temperature on the properties of Ga-doped ZnO by pulsed laser deposition," *Thin Solid Films*, vol. 513, pp. 90–94, 2006.

[29] X.-L. Chen, J.-M. Liu, J. Ni, Y. Zhao, and X.-D. Zhang, "Wide-spectrum Mg and Ga co-doped ZnO TCO thin films for solar cells grown via magnetron sputtering with H_2 introduction," *Applied Surface Science*, vol. 328, pp. 193 – 197, 2015.

[30] C.-S. Tian, X.-L. Chen, J.-M. Liu, D.-K. Zhang, C.-C. Wei, Y. Zhao, and X.-D. Zhang, "Wide-spectrum Mg and Ga co-doped ZnO - TCO thin films with introduced hydrogen grown by magnetron sputtering at room temperature," *Applied Surface Science*, vol. 314, pp. 786 – 793, 2014.

[31] I.-S. Kim, J. S.-H., and B.-T. Lee, "Growth and characterization of high quality homoepitaxial ZnO films by rf magnetron sputtering," *Semicond. Sci. Technol.*, vol. 22, pp. 683–686, 2007.

[32] K. Furusawa, H. Nakasawa, Y. Ishikawa, and S. F. Chichibu, "Homoepitaxial growth of ZnO films with reduced impurity concentrations by helicon-wave-excited-plasma sputtering epitaxy using a crystalline ZnO target prepared by hydrothermal technique," *Japanese Journal of Applied Physics*, vol. 53, no. 10, p. 100301, 2014.

[33] S. Zhu, C.-H. Su, S. L. Lehoczky, M. T. Harris, M. J. Callahan, P. McCarty, and M. A. George, "Polarity effects of substrate surface in homoepitaxial zno film growth," *Journal of Crystal Growth*, vol. 219, no. 4, pp. 361 – 367, 2000.

[34] K. Ellmer, "Magnetron sputtering of transparent conductive zinc oxide: Relation between the sputtering parameters and electronic properties," *J. Phys. D: Appl. Phys.*, vol. 33, pp. R17–R32, 2000.

[35] B. Chapman, *Glow discharge processes: Sputtering and plasma etching.* John Wiley & Sons, Inc., 1980.

[36] M. Birkholz, P. F. Fewster, and G. C., *Thin Film Analysis by X-Ray Scattering.* WILEY-VCH, 2006.

[37] R. Cebulla, R. Wendt, and K. Ellmer, "Al-doped zinc oxide films deposited by simultaneous rf and dc excitation of a magnetron plasma: Relationships between plasma parameters and structural and electrical film properties," *J. Appl. Phys.*, vol. 83, pp. 1087–1095, JAN 15 1998.

[38] V. M. Kaganer, O. Brandt, A. Trampert, and K. H. Ploog, "X-ray diffraction peak profiles from threading dislocations in GaN epitaxial films," *Physical Review B*, vol. 72, no. 045423, 2005.

[39] Y. J. Sun, O. Brandt, T. Y. Liu, A. Trampert, K. H. Ploog, J. Bläsing, and A. Krost, "Determination of the azimuthal orientational spread of GaN films by x-ray diffraction," *Appl. Phys. Lett.*, vol. 81, no. 26, pp. 4928–4930, 2002.

[40] T. Lei, K. F. Ludwig, and T. D. Moustakas, "Heteroepitaxy, polymorphism, and faulting in GaN thin films on silicon and sapphire substrates," *Journal of Applied Physics*, vol. 74, no. 7, pp. 4430–4437, 1993.

[41] V. L. Mironov, *Fundamentals of Scanning Probe Microscopy.* The Russian Academy of Sciences, 2004.

[42] Y. Leng, *Materials Characterization - Introduction to Microscopic and Spectroscopic Methods.* John Wiley & Sons (Asia) Pte Ltd, 2008.

[43] F. J. Giessibl, "High-speed force sensor for force microscopy and profilometry utilizing a quartz tuning fork," *Appl. Phys. Lett.*, vol. 73, no. 26, pp. 3956–3958, 1998.

[44] F. J. Giessibl, F. Pielmeier, T. Eguchi, T. An, and Y. Hasegawa, "Comparison of force ssensor for atomic force microscopy based on quartz tuning forks and length extensional resonators," *Phys. Rev. B: Condens. Matter Mater. Phys.*, vol. 84, no. 125409, 2011.

[45] T. R. Albrecht, P. Grütter, D. Horne, and D. Rugar, "Frequency modulation detection using high-Q cantilevers for enhanced force microscope sensitivity," *J. Appl. Phys.*, vol. 69, no. 2, pp. 668–673, 1991.

[46] L. Palmetshofer, "Rutherford Backscattering Spectroscopy (RBS)," in *Surface and Thin Film Analysis* (G. Friedbacher and H. Bubert, eds.), ch. 11, pp. 191–202, Wiley-VCH Verlag GmbH & Co. KGaA, 2011.

[47] H. Bakhru, "Rutherford Backscattering Spectroscopy," in *Encyclopedia of Materials: Science and Technology (Second Edition)* (K. H., J. Buschow, R. W. Cahn, M. C. Flemings, B. Ilschner, E. J. Kramer, S. Mahajan, and P. Veyssière, eds.), pp. 8242 – 8247, Oxford: Elsevier, second edition ed., 2001.

[48] G. D. Gilliland, "Photoluminescence spectroscopy of crystalline semiconductors," *Materials Science and Engineering: R: Reports*, vol. 18, pp. 99 – 399, 1997.

[49] W. Y. Liang, "Excitons," *Physics Education*, vol. 5, no. 4, pp. 226–228, 1970.

[50] R. Krüger-Sehm, "Stylus profilometry," in *Encyclopedia of Tribology* (Q. J. Wang and Y. W. Chung, eds.), pp. 3370–3376, Springer US, 2013.

[51] L. J. van der Pauw, "A method of measuring specific resistivity and hall effect of discs of arbitrary shape," *Philips Research Reports*, vol. 13, pp. 1–9, 1958.

[52] F. M. Smits, "Measurement of Sheet Resistivities with the Four-Point Probe," *Bell System Technical Journal*, vol. 37, no. 3, pp. 711–718, 1958.

[53] L. B. Valdes, "Resistivity Measurement on Germanium for Transistors," *Proceedings of the IRE*, February 1954.

[54] K. Maeda, M. Sato, I. Niikura, and T. Fukuda, "Growth of 2 inch zno bulk single crystal by the hydrothermal method," *Semicond. Sci. Technol.*, vol. 20, no. 4, p. S49, 2005.

[55] K. Matsumoto, K. Kuriyama, and K. Kushida, "Electrical and photoluminescence properties of carbon implanted ZnO bulk single crystals," *Nuclear Instruments and Methods in Physics Research Section B: Beam Interactions with Materials and Atoms*, vol. 267, no. 8-9, pp. 1568 – 1570, 2009. Proceedings of the 16th International Conference on Ion Beam Modification of Materials.

[56] T. M. Børseth, B. G. Svensson, A. Y. Kuznetsov, P. Klason, Q. X. Zhao, and M. Willander, "Identification of oxygen and zinc vacancy optical signals in ZnO," *Appl. Phys. Lett.*, vol. 89, no. 26, pp. –, 2006.

[57] K. T. Roro, J. K. Dangbegnon, S. Sivaraya, A. W. R. Leitch, and J. R. Botha, "Influence of metal organic chemical vapor deposition growth parameters on the luminescent properties of ZnO thin films deposited on glass substrates," *J. Appl. Phys.*, vol. 103, no. 5, pp. –, 2008.

[58] H. Kato, M. Sano, K. Miyamoto, and T. Yao, "Growth and characterization of Ga-doped ZnO layers on a-plane sapphire substrates grown by molecular beam epitaxy," *Journal of Crystal Growth*, vol. 237-239, Part 1, pp. 538 – 543, 2002. The thirteenth international conference on Crystal Growth in conj unction with the eleventh international conference on Vapor Growth and Epitaxy.

[59] A. Bikowski and K. Ellmer, "Influence of the deposition temperature on electronic transport and structural properties of radio frequency magnetron-sputtered $Zn_{1-x}Mg_xO$:Al and ZnO:Al films," *Journal of Materials Research*, vol. 27, pp. 2249–2256, 2012.

[60] K. Ellmer and R. Mientus, "Carrier transport in polycrystalline transparent conductive oxides: A comparative study of zinc oxide and indium oxide," *Thin Solid Films*, vol. 516, no. 14, pp. 4620 – 4627, 2008. 6th International Conference on Coatings on Glass and Plastics (ICCG6)- Advanced Coatings for Large-Area or High-Volume Products-.